Effect of different femur shapes on the development of cam-type deformities

The development of a combined bone growth and remodeling algorithm to investigate the effect of different femur shapes generated by a SSAM on the development of cam-type deformities

N.H.A. Rutten

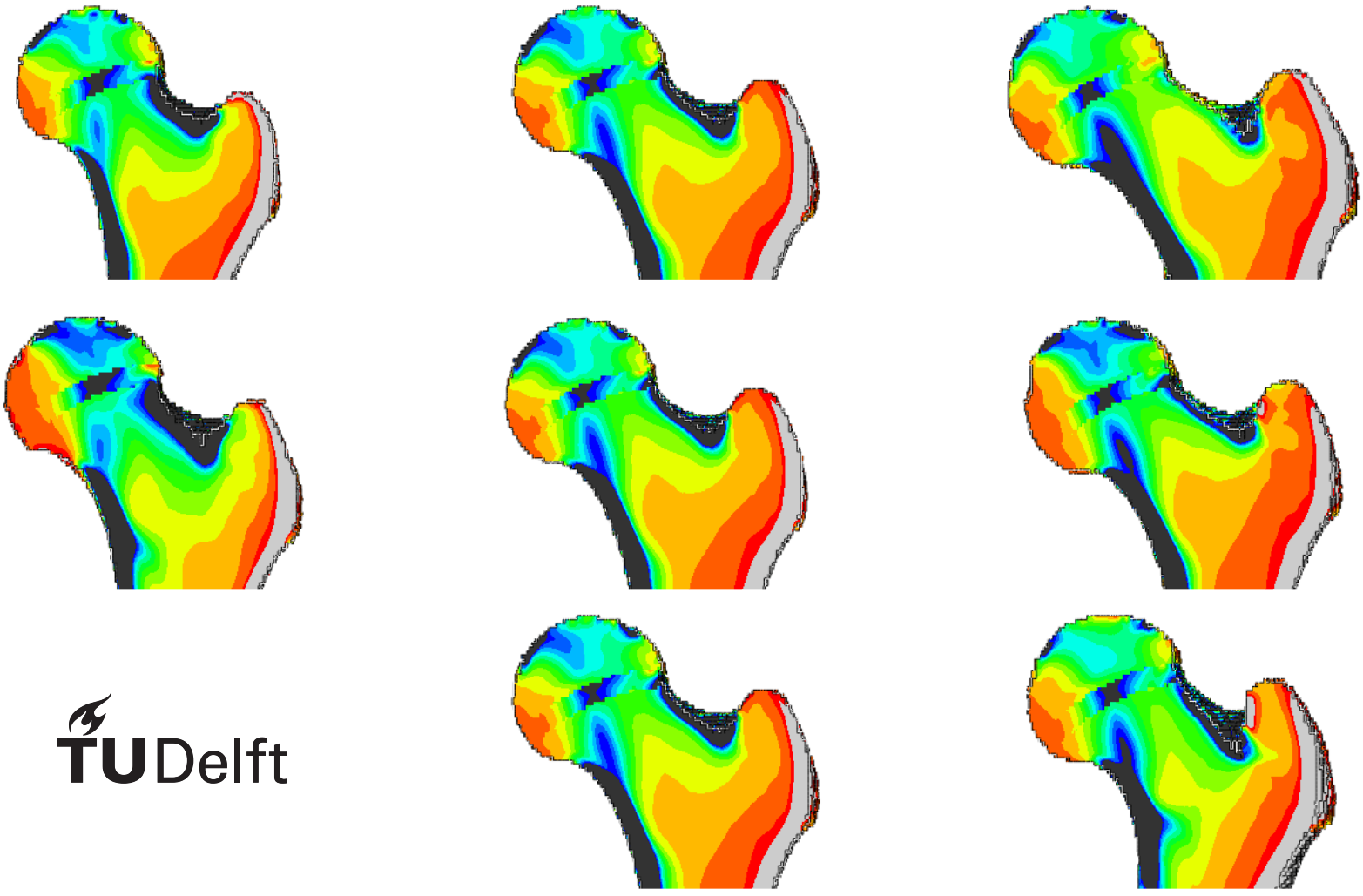

TU Delft

Effect of different femur shapes on the development of cam-type deformities

The development of a combined bone growth and remodeling algorithm to investigate the effect of different femur shapes generated by a SSAM on the development of cam-type deformities

by

N.H.A. Rutten

to obtain the degree of Master of Science
at the Delft University of Technology,
to be defended publicly on Thursday September 9, 2021 at 11:00 AM.

Student number:	4288394	
Project duration:	June 8, 2010 – July 13, 2021	
Thesis committee:	Prof. dr. A.A. Zadpoor,	TU Delft, supervisor
	Dr. Ir. N. Tumer,	TU Delft, supervisor
	Dr. A.C. Akyildiz,	TU Delft and Erasmus MC

TU Delft

Abstract

Introduction: A combined bone growth and remodeling model should be created, to investigate the effect of different femur shapes on the risk of developing cam type deformities. The different femur shapes needed for this study can be created using a statistical shape and appearance model (SSAM). The workflow of the combined bone growth and remodeling model has been (semi-)automated for increased efficiency and other future uses.

Methods: An algorithm was created that leads the user through a (semi-)automated workflow, where the necessary features are added to the simulation. The model uses remodeling and growth simulations in sequence to estimate both the change in density distribution and in shape. The used loading conditions correspond to the 10% gait cycle phase. The remodeling is driven by strain energy density, and the growth by the osteogenic index.

Results: The resulting density distributions are similar to those found in other studies, while the growth model predicts larger changes in the neck axis angle than other studies. The growth was also predicted for two MRI pilot scans and the predicted growth was similar to the growth found in follow up scans of the same children. To investigate the influence of the bone shape on the development on cam deformities, three different shape modes were varied and their influence on the osteogenic index in the growth plate was analyzed. The results from this study indicate that an increased femoral neck-axis angle increase the growth stimulation in the cam region of the growth plate.

Discussion: The created bone adaptation model performs mostly as expected, only the included growth model occasionally performs unreliably. To improve its reliability, recommendations have been given to improve its behaviour. Because of the increased growth stimulation in the cam region of the growth plate, the results indicate that femurs with a large neck-axis angle have an increased risk of developing cam type deformities. The effect of other shape characteristics is unclear, and more research is recommended to investigate the effect of other characteristics, such as the femoral anteversion.

Preface

The basis of this research was my great interest in the biomechanics behind bone adaptation. Bone is an incredibly interesting and adaptive material that a great amount of information can be obtained from. The adaptive properties of bone can be simulated in lots of different ways and at different scales. I learnt a lot about bone during both my literature study and my graduation project, in which I spent the large majority of the time developing the combined bone growth and remodeling model.

The COVID-19 pandemic was perhaps one of the hardest times to graduate: almost all contact was remote through video meetings and desktops had to be shared using a remote connection. Working from home, during these trying times was sometimes hard, however the challenges created by the pandemic have learnt me a lot. From the importance of regular meetings to how to organize a workplace.

In the end, I could not have finished this graduation project at the same quality without a great support structure. Firstly, I would like to thank my daily supervisor Dr. Ir. N. Tumer, for her continued support and guidance throughout the research process. Additionally, I would like to thank her for offering a listening ear and providing useful hints and tips on how to work more efficiently. I would also like to thank Prof. Dr. A.A. Zadpoor for his guidance and critical attitude. Additionally, I would like to thank Dr. R. Agricola for providing the MRI-scans, which were incredibly useful for the growth validation. I would also like to thank him/her for providing his/her experience on the development of cam-type deformities.

Lastly, I would like to thank my loving family, partner and friends. I would like to thank my parents and my brother for their love, support and infinite wisdom. I would also like to thank my partner for her love, support and listening ear. Lastly, I would like to thank all my friends who were there remotely, or more close-by, for their advice and support.

Thank you to all for your support, in every form imaginable.

N.H.A. Rutten
Delft, July 2021

Contents

Nomenclature

Abbreviation	Explanation
ANN	Artificial neural network
BW	Body weight
CT(-scan)	Computed tomography (scan)
FA	Femoral anteversion
FE(A)	Finite element (analysis)
FNDD	Femoral neck shaft axis deflection direction
HCF	Hip contact force
LR	Linear regression
MRI(-scan)	Magnetic resonance imagining (scan)
NAA	Neck axis angle
OI	Osteogenic index
PSD	Principal stress direction
QCT(-scan)	Quantitative computated tomography (scan)
SED	Strain energy density
SSAM	Statistical shape and appearance model
STD	Standard deviation

Symbol	Explanation	Unit	Topic	Section
γ	Power law, exponential constant	[-]	Material model	section 2.5
$\boldsymbol{\epsilon}$	Strain component vector	[-]	Remodeling	section 2.6
$\dot{\epsilon}$	Growth rate	[-]	Growth	section 2.7
$\dot{\epsilon}_b$	Biological growth rate	[-]	Growth	section 2.7
$\dot{\epsilon}_m$	Mechanical growth rate	[-]	Growth	subsection 2.7.1
ρ	Density	[g*cm^{-3}]	Material model	section 2.5
$\boldsymbol{\sigma}$	Stress component vector	[MPa]	Remodeling	section 2.6
σ_{Hi}	Hydrostatic stress	[MPa]	Growth	subsection 2.7.1
σ_{Si}	Octahedral shear stress	[MPa]	Growth	subsection 2.7.1
$\boldsymbol{\sigma}_{\mathbf{p}}$	Principal stress vector	[MPa]	Growth	subsection 2.7.1
Φ_i	Weighted remodeling stimulus	[J/g]	Remodeling	section 2.6
$\boldsymbol{\Phi}_{\mathbf{G}}$	Shape mode variation matrix	[mm]	Image generation	subsection 2.3.1
$\boldsymbol{\Phi}_{\mathbf{s}}$	Appearance mode variation matrix	[HU]	Image generation	subsection 2.3.1
a	Growth stimulation constant	[-]	Growth	subsection 2.7.1
b	Growth inhibition constant	[-]	Growth	subsection 2.7.1
B	Remodeling time constant	[-]	Remodeling	section 2.6
$\vec{\mathbf{b}}_{\mathbf{G}}$	Apperance parameters	[-]	Image generation	subsection 2.3.1
$\vec{\mathbf{b}}_{\mathbf{s}}$	Shape parameters	[-]	Image generation	subsection 2.3.1
C	Power law, linear constant	[-]	Material model	section 2.5
c_g	Growth amplification factor	[-]	Growth	subsection 2.7.2
D	Osteocyte distance coefficient	[mm]	Remodeling	section 2.6
$d(x)$	Distance between two elements	[mm]	Remodeling	section 2.6
E	Young's modulus	[MPa]	Material model	section 2.5
$\mathbf{e}$	Growth expansion coefficients	[-]	Growth	subsection 2.7.2
f_i	Exponential distance function	[-]	Remodeling	section 2.6
$\mathbf{G}$	Bone appearance	[HU]	Image generation	subsection 2.3.1
k	Remodeling stimulus reference value	[J/g]	Remodeling	section 2.6
l	Lazy zone size	[-]	Remodeling	section 2.6
l_1	Growth layer thickness in [1]	[mm]	Growth	subsection 2.7.2
l_2	Growth layer thickness in current study	[mm]	Growth	subsection 2.7.2
$N_{el,incl}$	Number of nearby elements included in $f_i(x,t)$	[-]	Remodeling	section 2.6
R	(Sphere) radius	[mm]	Growth plate generation	subsection 2.3.3
r_i	Distance between sphere centroid and element i	[mm]	Growth plate generation	subsection 2.3.3
S_i	Local remodeling stimulus of element i. $S_i = U_i/\rho_i$	[J/g]	Remodeling	section 2.6
$\mathbf{u}_{\mathbf{g,i}}$	Growth direction	[-]	Growth	subsection 2.7.2
$\mathbf{u}_{\boldsymbol{\sigma}_{\mathbf{p1,i}}}$	Direction of first principal stress	[-]	Growth	subsection 2.7.2
U_i	Strain energy density of element i	[MPa]	Remodeling	section 2.6
$\mathbf{x}$	Bone shape	[mm]	Image generation	subsection 2.3.1

1 Introduction

Bone is an adaptive tissue that is influenced by and exerts influence on the surrounding environment. These adaptive properties can be modeled in a forward model, in which the environment determines the bone properties. These models differ based on their scale, this is because the important mechanics are dependent on the scale, environment and what behaviour is of interest. The process where bone tissue is replaced by new bone tissue is called remodeling, and the process where bone grows in the growth plate is called (longitudinal) growth. This research aims to provide information on how different femur shapes influence the development of cam type deformities by examining the local growth stimulation in the growth plate and by performing forward bone adaptation simulations. To do this the algorithm must generate new bone morphologies (i.e. shape and appearance), and create and perform the subsequent growth and remodeling simulations (semi-)automatically.

This chapter will introduce the background of this research as well as the research itself. First the background will be presented in section 1.1, after which the research problem is explained in section 1.2. The research questions are discussed in section 1.3. Following this the significance, section 1.4, is discussed. The chapter concludes with a structural outline of the entire thesis in section 1.5.

1.1. Background

Bones perform multiple key functions in the human body, such as providing support, assisting movement, protecting vital organs, being a mineral and triglyceride reserve and blood cell production [2]. Due to the adaptive properties of bone, important information on the state of the human body can be obtained from examining bones [3–5]. One of these adaptive properties is known as Wolff's Law [5], which says that the structure of bone is optimized for the loading conditions it faces. The current study relates to its function of providing support, assisting movement and indirectly its function as a mineral reserve.

1.1.1. Remodeling models

As stated previously, bone remodeling is the local replacement of old bone tissue by new bone tissue. This process can change the local mechanical properties of the bone by replacing old bone tissue for new bone tissue. Biologically, bone remodeling occurs during multiple phases, this process can be seen in Figure 1.1. The first phase of remodeling is the activation phase, where the osteocytes activate the osteoclasts. In the resorption phase, the osteoclasts perform resorption of bone tissue. During the reversal phase pre-osteoblasts attach to the bone surface. During the formation phase, osteoblasts perform apposition of new bone tissue. And in the final phase, quiescence, osteoblasts attached to the bone surface become bone lining cells. In short: the osteocyte senses that bone should be replaced in a certain location, the osteoclast then removes bone tissue in that location and the osteoblast then deposits new bone tissue. This process can be approximated by a change in the bone apparent density. For more information on the biological process of remodeling, the reader is referred to Allen et al [4] and Bellido et al [3].

This bone apparent density is an approximation of the bone density at continuum scale: complex micro-structures are replaced by a simplified 1D measure. This bone apparent density is a measure

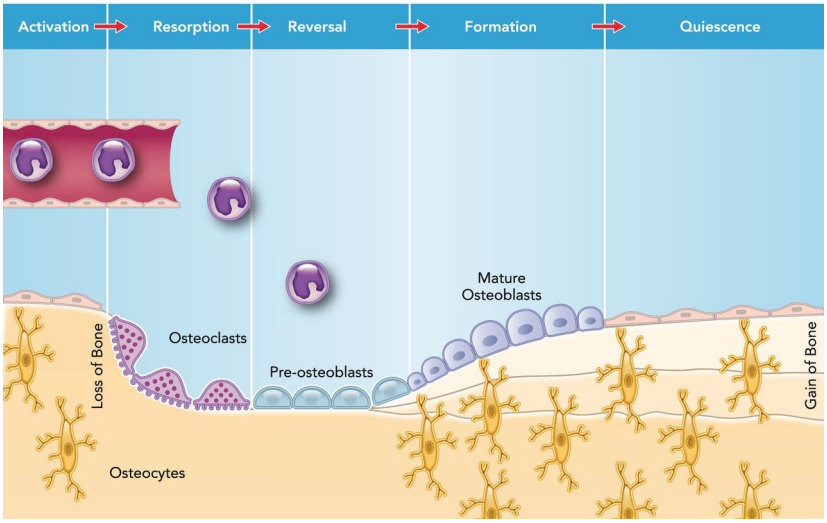

Figure 1.1: A simplified overview of the different phases during the remodeling process. The first two phases are the activation of osteoclasts, and the resorption of bone tissue by the osteoclasts. The third phase is the attachment of pre-osteoblasts to the newly exposed bone tissue. The fourth phase is the formation of new bone tissue by the osteoblasts. This figure was obtained from [6].

of how much bone tissue is in a location, where a higher bone apparent density results in stiffer bone, and a lower bone apparent density results in more flexible bone.

1.1.2. Growth models

The longitudinal growth in the bones of children takes place in the growth plate, also known as the epiphyseal plate. In this thin bone region, bone cells perform mitosis (cell multiplication) and tissue generation in the direction of growth. According to [7–10], certain stresses in the growth plate inhibit growth, while others stimulate growth. This influence of the mechanical environment on growth is local and therefore influences both the magnitude of growth, as well as its direction. The most commonly used mathematical theory is that of osteogenic index, a weighted sum of the local octahedral shear stress (stimulating) and the hydrostatic stress (inhibiting).

Biological factors also have a large influence on longitudinal growth. Growth can be affected by genetic factors, hormones, diet and age. These factors are often simplified and approximated as a constant biological growth component, which is added to the osteogenic index to obtain the local growth magnitude.

The growth direction is influenced by the stresses as well, and can be approximated in two ways: the direction of deflection [1] and the direction of the maximum principal stresses [11]. The direction of deflection does not model local differences in growth direction. The principal stress direction method has recently been used successfully [11] and is able to model local differences in growth direction.

Growth is often modeled using a multi-layered disc [1, 11], where the layers are grown one-by-one over multiple simulations. Manual remeshing is required to create both the disc and its multiple layers, which significantly increases the amount of time needed to create growth simulations.

1.1.3. Statistical Shape and Appearance Models

A method of artificially creating new bone shapes and density distributions is using a statistical shape and appearance model (SSAM) [12]. SSAMs use the mean and variance from a set of real bones, obtained using an imaging technique, such as CT-scans, to generate new shapes and appearances. In a SSAM, the shape parameters determine the external shape of the bone, while the appearance parameters relate to the density distribution of the generated bone.

1.2. Research Problem

A previous study, Roels et al [13], investigated the influence of different loading conditions and growth plate orientations on the development of cam deformities. A cam deformity is a deformation

in the femur head, resulting in a non-spherical femur head. This is believed to increase the risk of developing hip osteoarthritis [14]. Cam deformities are believed to be caused by excessive growth in the cam region of the growth plate [13–18]. The influence of different femur shapes is currently unknown and could provide useful insights and could improve cam deformity risk assessment.

1.3. Research Aims, Objectives and Questions

This study aims to increase the knowledge on the effect different femur shapes have on the risk of developing cam type deformities.

1.3.1. Aims and Objectives

The objectives for the study are to create different morphologies associated with the shape modes of interest. Next, for these different shapes, the local growth stimulation in the growth plate will be examined and analyzed. Subsequently, the shapes that have an increased risk of developing cam-type deformities will be further discussed. A combined bone growth and remodeling algorithm should be used to assess both the development of the bone shape and to obtain a realistic bone density distribution, that adapts to changing loading conditions. For this study, a combined bone growth and remodeling algorithm will be used that was originally developed for the creation of an inverse bone adaptation model, however it can be used for other studies like these as well. The majority of this thesis concerns the development of this forward bone adaptation model.

1.3.2. Research Questions

For the study, the primary research question is: What femur shapes increase the risk of developing cam type deformations?

This research question can then be subdivided into: Of the different shape modes of the SSAM, which have a significant impact on the femur head and neck geometry? For these shape modes, what is their influence on the distribution of the osteogenic index in the growth plate? What shape modes result in an increased growth stimulation in the cam region of the growth plate?

1.4. Significance

Cam-type deformities increase the risk of hip osteoarthritis [13–18], however it is unclear how different shape variations influence the formation of cam-type deformities. Knowing what shapes have a higher likelihood of developing cam-type deformities can help with early detection and treatment.

1.5. Structural outline

This thesis introduces the research in this chapter, the introduction, where the background is first introduced and subsequently the research itself is explained. In chapter 2 Methods, the methodology of the study is presented. First it is explained how the mesh is created from the SSAM parameters, next what loading conditions were used and what material models are used for the different types of bone. Lastly, the remodeling and growth models are presented. The results are then divided into three chapters related to the remodeling (chapter 3), the growth (chapter 3) and the influence of shape modes on cam deformity risk (chapter 5). The chapter on remodeling results contains a mesh convergence study, sensitivity analysis and qualitative comparison to other studies. The chapter on growth results contains a mesh convergence study and sensitivity analysis as well, additionally it contains a MRI-scan validation where real growth in two children is compared to the predicted growth by the model. The chapter on SSAM shape modes influence on the cam deformity risk, contains the osteogenic index distributions for different shape modes, and the influence is then discussed. Chapter 6 Discussion contains the limitations and evaluation of the research as well as future recommendations and the conclusion.

2

Methods

A forward bone growth and remodeling model consists of multiple different components, performing different functions. In this chapter these different components are presented, including information on how they are implemented. This chapter starts with an overview of these different components and their function. Subsequently, all components are individually presented.

2.1. Overview

The different components are the statistical shape and appearance model, growth plate generation algorithm, the used loading conditions, the used material models, bone remodeling algorithm and bone growth algorithm. The statistical shape and appearance model is used to generate new bone morphologies from shape and appearance parameters. The growth plate generation algorithm creates the growth plate region from the bone morphology. The section on loading conditions presents the loading scenarios used in this study and the section on material models explains the material behaviour of cortical and trabecular bone, as well as the growth plate. The section on bone remodeling algorithm and the section on bone growth have information on the used algorithms and how they were implemented.

2.2. Software

For finite element analysis SIMULIA Abaqus 2017 was used, linked with the Intel Compiler 17.0 Update 6 and Microsoft Visual Studio Community 2013. For the final part of the project, SIMULIA Abaqus 2019 was used, linked with Intel OneAPI Toolkits, for the compiling of the Fortran scripts. The remodeling algorithm uses user-subroutines written in Fortran 95, which are written in Microsoft Visual Studio and compiled by the Intel Compiler. The original statistical shape and appearance model [19, 20] was rewritten from Python 2.7 to Python 3.7 and now utilizes SimpleITK 2.0.2. The SSAM uses Elastix [21, 22]. The growth plate generation algorithm was written in Python 3.7 and uses SciPy 1.5.2 for numerical optimization, as well as NumPy 1.19.2. The rest of the model is written in Python 3.7, and uses the following external packages: NumPy 1.19.2, Matplotlib 3.3.2 for visualizing results.

2.3. Statistical Shape and Appearance Model

The statistical shape and appearance model (SSAM) [12] used in this study has previously been established and used [19, 20]. The SSAM can generate new bone morphologies using shape and appearance parameters. The bone shape depends on the chosen shape parameters, while the bone density distribution depends on the used appearance parameters.

2.3.1. Image Generation

The SSAM used in this study describes the external femur shape using a point cloud, and describes the appearance using images in the raw format. The shape and appearance parameters therefore describe the relationships between the modes of variation and the point coordinates and pixel values.

New shapes are generated as follows [12]:

$$\vec{\mathbf{x}} = \hat{\mathbf{x}} + \mathbf{\Phi_s}\vec{\mathbf{b}}_\mathbf{s} \tag{2.1}$$

where $\vec{\mathbf{x}}$ is the generated shape, $\hat{\mathbf{x}}$ is the mean shape, $\mathbf{\Phi_s}$ is the matrix containing the main modes of variation of the shape from the average values and $\vec{\mathbf{b}}_\mathbf{s}$ is the vector containing the shape parameters that relate to the different modes of variation of the shape.

The new appearance is generated in a similar fashion:

$$\mathbf{G} = \hat{\mathbf{G}} + \mathbf{\Phi_G}\mathbf{b_G} \tag{2.2}$$

where $\mathbf{G}$ is the new appearance, $\hat{\mathbf{G}}$ is the mean appearance, $\mathbf{\Phi_G}$ is main modes of variation of the density distribution from the average values and $\mathbf{b_G}$ is the matrix containing the appearance parameter values for the different modes of variation.

To combine the generated shape with the generated appearance, Elastix [21, 22] is used to calculate the transform from the mean shape to the generated shape. This transform is then applied to the generated appearance image, resulting in a generated bone morphology with a new shape and appearance.

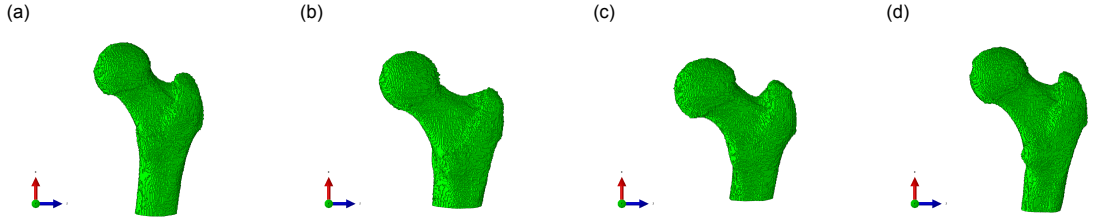

Figure 2.1: Different shapes of the proximal femur after conversion to an Abaqus model. These shapes have been created using the SSAM [19, 20].

2.3.2. Mesh Generation

The next step is to convert the generated image file into a volumetric voxel mesh. This is done by first cropping the image file to the smallest cubic space that fits the femur. For this study, the growth and remodeling in the proximal femur was of interest, and therefore only the top $2/7^{\text{th}}$ of the femur was included. At this point a reduction factor is introduced to decrease the number of elements that are created, which is done to increase the computational efficiency of the model. A reduction factor of 2 generally results in 50,000 to 65,000 elements. This was done using the Scipy package, and the function ndimage.zoom, which rescales a matrix and recalculates the index values. Next, all possible node coordinates are generated, based on the image size and spacing. Subsequently, the background is filtered out, and for all pixel values larger than the background an element is created. Some shapes created with the SSAM and turned into Abaqus models can be found in Figure 2.1.

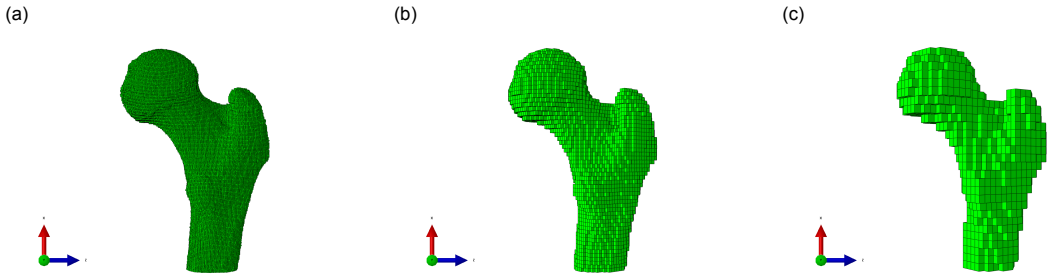

Figure 2.2: Three different meshes created from one shape, with the reduction factor being: a) 1.0, which means every pixel in the image has been turned into an element; b) 8.0; and c) 64.0. For all reduction factors, the shape of the femur remains intact, however details disappear for higher reduction factors.

When the entire mesh has been generated, it is then written into an Abaqus input file, which can be imported into Abaqus. This requires the nodal coordinates and the element to node connectivity.

2.3.3. Growth Plate Generation

Next, the growth plate region needs to be defined. The growth plate is approximated to have a spherical shape, as done by Roels et al [13]. The user needs to manually create two sets of nodes in Abaqus, one of which contains the nodes in the larger region surrounding the growth plate, and one that contains an approximation of the growth plate shape. The nodes to select are shown in Figure 2.3

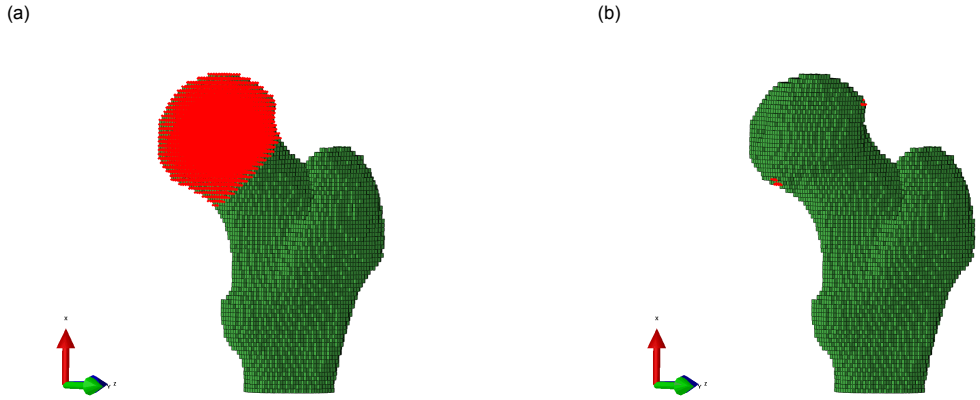

Figure 2.3: The selection of two node sets is shown to indicate the locations of these sets. a) the first node set is the HEADNECKNODES, which contains nodes in the femoral head and where it transitions into the neck. This region will contain the growth plate, and the algorithm will restrict itself from only creating the growth plate in this region. b) The nodes selected to general position of the growth plate. The algorithm will optimize the location and orientation of the growth plate center, so that the outer surface intersects with the selected nodes.

This second set can be defined using as few as two nodes, at the lateral and medial sides of the growth plate. A sphere is then fitted to the selected nodes, so that the radius and sphere center coordinates, C, are calculated. Finally, the growth plate region will include all elements in the first set that are within a distance ΔR_{max}, of the outer surface of the sphere, such that:

$$\Delta R_i = |R - r_i| \leq \Delta R_{max} \tag{2.3}$$

where R is the radius of the sphere, r_i is the distance between the centroid of element i and the sphere center, and ΔR_i is the absolute difference between the two. The resulting growth plate sets, both for nodes and elements, are shown in Figure 2.4.

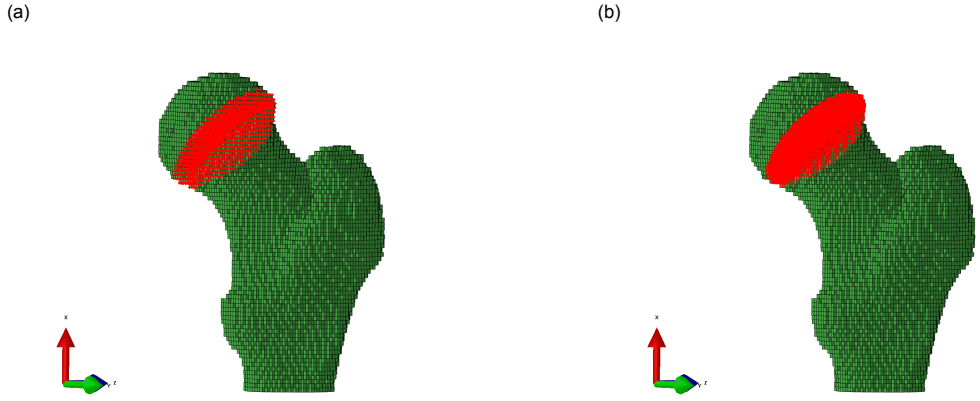

Figure 2.4: The created a) node set and b) element set for the growth plate. This set is created using the sets created in Figure 2.3, using Equation 2.3

2.4. Loading Conditions

The loading conditions used were adapted from Bitsakos et al. [23], as used in Campoli et al. [24]. The loads used are in accordance with the 10% cycle of gait step from [23], and can be found in Table 2.1. The loads are adapted to percentage body weight, so that they can be used for children. The

Table 2.1: The load magnitudes and directions of the used joint contact and muscle forces, obtained from [23] and scaled to a body weight of 735 N, in accordance with [24].

Load	Magnitude [%BW]	e_x	e_y	e_z
Hip contact force	267.5	0.206	0.436	-0.876
Gluteus maximus	55.88	0.0915	-0.572	0.815
Gluteus medius	44.06	-0.176	-0.570	0.802
Gluteus minimus	10.32	-0.176	-0.579	0.796
Piriformis	11.92	0.297	-0.865	-0.405
Adductor magnus	25.93	0.132	-0.409	0.903
Adductor minimus	9.644	-0.168	-0.838	0.519

forces included in the 10 % gait cycle are the hip contact force and the following muscle forces: gluteus maximus, gluteus medius, gluteus minimus, piriformis and adductor magnus and adductor minimus. In Figure 2.5 the surfaces that need to be created are visualized. After creating these surfaces in the model, their surface areas should be added to a text file which is automatically opened. This should be done in the order described above and that of Figure 2.5.

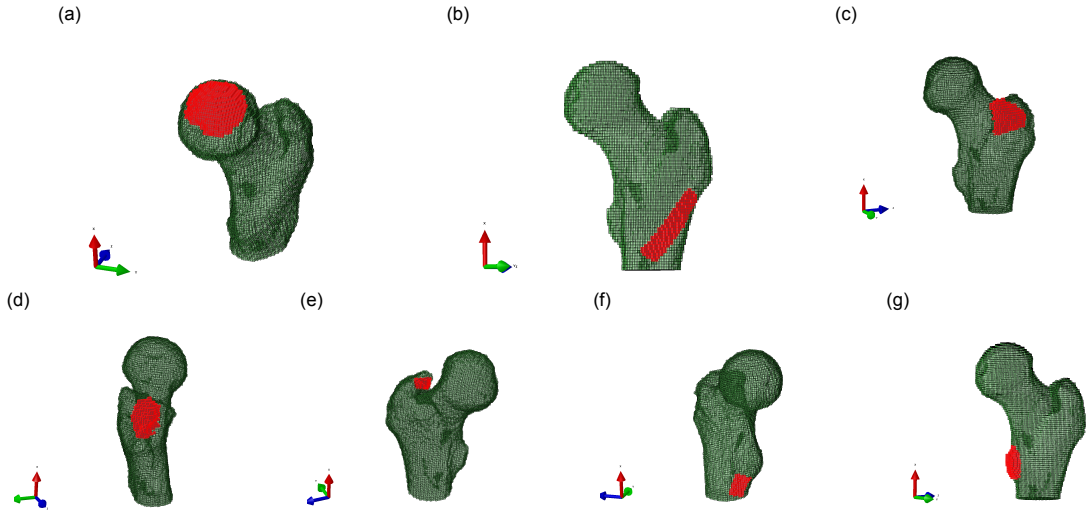

Figure 2.5: The highlighted surfaces indicate the region where the surfaces should be created for the following loads: a) the hip contact force (HCF); b) the gluteus maximus; c) the gluteus medius; d) the gluteus minimus; e) the piriformis; f) the adductor magnus; and g) the adductor minimus. The associated magnitudes and directions of the loads can be found in Table 2.1.

2.5. Material Model

The chosen material model is an isotropic linear elastic model, which uses the power law [25] for the relationship between bone density and the stiffness of the bone. This power law is described as [25]:

$$E = C * \rho^{\gamma} \tag{2.4}$$

where E is the Young's modulus in MPa, C is a constant, ρ is the apparent bone density in g/cm^{-3}and γ is the power constant. For the used material model, the values of C, and γ are dependent on the bone apparent density. For $0.01 \leq \rho \leq 1.2$ the bone is assumed to be trabecular bone, and for $1.2 \leq \rho \leq 2.0$ the bone is regarded to be cortical bone. The values used for the trabecular bone are C_t, γ_t, with a poissons ratio, ν_t, of which the values can be found in Table 2.2. For cortical bone C_c, γ_c and ν_c, are used, and their values can also be found in Table 2.2. The parameter values used in this study are from previous studies [26–29].

Table 2.2: An overview of the parameter values used for the material model.

Parameter	Value	Unit	Parameter	Value	Unit
ρ_{min}	0.01	g∗cm^{-3}	γ_t	2.5	-
ρ_{max}	2.0	g∗cm^{-3}	γ_c	3.2	-
ρ_{tc}	1.2	g∗cm^{-3}	ν_t	0.2	-
C_t	2014	-	ν_c	0.32	-
C_c	1763	-			

2.6. Bone Remodeling

The used internal remodeling model used here is based on the strain energy density, as proposed by [30, 31] and used for inverse bone remodeling models by [32–37]. This strain energy density is divided by the bone apparent density, as proposed by Huiskes et al [31]:

$$S_i(x,t) = \frac{U_i(x,t)}{\rho_i(x,t)} \tag{2.5}$$

where $S_i(x,t)$ is the mechanical stimulus, $\rho_i(x,t)$ is the bone apparent density, $U_i(x,t)$ is the strain energy density as defined by:

$$U_i(x,t) = \frac{1}{2}\overrightarrow{\boldsymbol{\epsilon}_\mathbf{i}}(x,t)\overrightarrow{\boldsymbol{\sigma}_\mathbf{i}}(x,t) \tag{2.6}$$

where $\overrightarrow{\boldsymbol{\epsilon}_\mathbf{i}}(x,t)$ is the vector containing the strain components and $\overrightarrow{\boldsymbol{\sigma}_\mathbf{i}}(x,t)$ is the vector containing all the stress components.

The remodeling algorithm has a spatial influence that simulates the sensing function of the osteocytes, which senses the mechanical stimulus in nearby surrounding bone tissue. This method was proposed by Mullender et al [38, 39], in the original theory the remodeling signal then became:

$$\Phi_i(x,t) = \frac{\sum_{i=1}^{N} f_i(x)(S_i(x,t) - k)}{\sum_{i=1}^{N} f_i(x)} \tag{2.7}$$

where $\Phi_i(x,t)$ is the remodeling signal, N is the number of elements in the model, k is a reference signal constant, $f_i(x)$ is an exponential function:

$$f_i(x) = e^{-d(x)/D} \tag{2.8}$$

where $d(x)$ is the distance between two elements and D is a parameter influencing the decay of the sensing strength. Lower values for D result in closer elements being relatively more influential than for higher values of D.

The original theory [30–32, 38, 39] did not include a lazy-zone in which bone remodeling does not occur when the mechanical signal is close to the reference signal.

If one were to include all elements in the model for the osteocyte distance function, for every element, the calculation would become computationally inefficient, because distant elements have nearly no effect, because their f_i value would become very low. Therefore the closest $N_{el,incl}$ elements are selected for every element. In that case, Equation 2.7, becomes:

$$\Phi_i(x,t) = \frac{\sum_{i=1}^{N_{el,incl}} f_i(x)S_i(x,t)}{\sum_{i=1}^{N_{el,incl}} f_i(x)} \tag{2.9}$$

And then the remodeling rate becomes:

$$\frac{d\rho(x,t)}{dt} = \begin{cases} B(\Phi_i(x,t) - (1-l)k) & \text{if } \Phi_i(x,t) < (1-l)k \\ 0 & \text{if } (1-l)k \leq \Phi_i(x,t) \geq (1+l)k \\ B(\Phi_i(x,t) - (1+l)k) & \text{if } \Phi_i(x,t) > (1+l)k \end{cases} \tag{2.10}$$

with B being the time constant, l is the lazy zone size and k is the reference value in J/g. Equation 2.10 is visually represented in Figure 2.6.

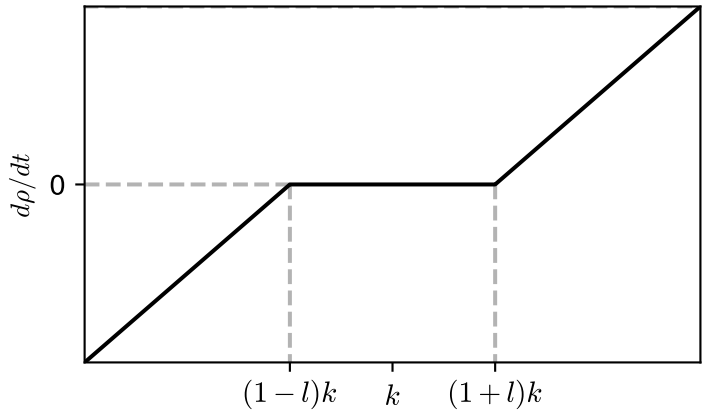

Figure 2.6: This figure contains the graphical representation of Equation 2.10, which contains the relationship between the mechanical signal, strain energy density divided by the apparent density, and the infinitesimal change in the apparent bone density.

The discretized change in the apparent bone density is then:

$$\Delta\rho(x,t) = \frac{d\rho(x,t)}{dt}\Delta t \tag{2.11}$$

And the new apparent bone density becomes:

$$\rho(x,t+1) = \rho(x,t) + \Delta\rho(x,t) \tag{2.12}$$

The values used for all parameters are given in Table 2.3 below. The values were determined using a sensitivity analysis, which can be found in section 3.2.

Table 2.3: An overview of the parameter values used for the remodeling algorithm.

Parameter	Value	Unit
B	50.0	-
S_{ref}	3.0×10^{-03}	[J/g]
l	0.3	-
D	1.0	[mm]
$N_{el,incl}$	50	-

2.6.1. Remodeling Algorithm

The remodeling algorithm consists of five main components, the Python script which manages the simulation and starts the analyses from the command window, the Abaqus finite element solver, the user-subroutine written in Fortran 95, a text file containing the initial apparent densities for all elements and a text file containing the values for $f_i(x)$, see Equation 2.8. To save information between elements the user-subroutine utilizes a module, which is a package which can be used to store data and functions. This module contains the remodeling parameters, paths to the text files, stimulus data for all elements, values of $f_i(x)$ for every element and the associated element numbers.

2.7. Bone Growth

Growth can be subdivided into biological growth and mechanical growth. Here the mechanical growth is dependent on the mechanical environment, while the biological growth is dependent on the biological environment. For this study, the biological growth is a constant, equal to 0.36 mm/step, as also found in [1], and used the method proposed by [10] and as used by Carriero et al [1] and Yadav et al [11]. The subdivided growth then becomes:

$$\dot{\epsilon} = \dot{\epsilon}_b + \dot{\epsilon}_m \tag{2.13}$$

2.7.1. Mechanical Growth

While the biological growth is often considered to be either constant or age-dependent, the mechanical growth can be calculated with [10]:

$$\dot{\epsilon}_m = a * \sigma_{Si} + b * \sigma_{Hi} \tag{2.14}$$

where a and b are constants, where the ratio b/a should be between 0.3 and 1 [1, 10, 11], and is often chosen to be 0.5 [1, 10, 11]. Additionally, a is chosen to be 0.02 month^{-1}MPa^{-1}, and b to be 0.01 month^{-1}MPa^{-1} [1, 10, 11]. σ_{Si} is the octahedral shear stress, defined as:

$$\sigma_{Si} = \frac{(\sigma_{p,1} - \sigma_{p,3})^2 + (\sigma_{p,1} - \sigma_{p,2})^2 + (\sigma_{p,2} - \sigma_{p,3})^2 +}{3} \tag{2.15}$$

and σ_{Hi} is the hydrostatic stress, defined as:

$$\sigma_{Hi} = \frac{\sigma_{p,1} + \sigma_{p,2} + \sigma_{p,3}}{3} \tag{2.16}$$

2.7.2. Growth Direction

Next the growth direction should be calculated, which was done using the direction of the maximum principal stress, first performed in Yadav et al [11]. This is done in the following way:

$$\mathbf{u_{g,i}}(x,t) = \frac{\mathbf{u}_{\sigma_{\mathbf{p1,i}}}(x,t)}{|\mathbf{u}_{\sigma_{\mathbf{p1,i}}}(x,t)|} \tag{2.17}$$

where $\mathbf{u_{g,i}}(x,t)$ is the growth direction and $\mathbf{u}_{\sigma_{\mathbf{p1,i}}}(x,t)$ is the direction of the maximum principal stress. This should then be multiplied with the growth magnitude to obtain the expansion coefficients.

In a previous study [1] a different growth plate thickness was used, and this should be compensated for. This is done using an added growth factor, c_g. The growth then becomes:

$$\overline{\mathbf{e}} = \begin{bmatrix} \mathrm{e}_x \\ \mathrm{e}_y \\ \mathrm{e}_z \end{bmatrix} = c_g \dot{\epsilon}\, \overline{\mathbf{u_g}} \tag{2.18}$$

with the growth factor, c_g defined as:

$$c_g = f\frac{l_1}{l_2} \tag{2.19}$$

where f is the amplification factor, l_1 is the growth layer thickness in Carriero et al [1], and l_2 is the current approximate growth plate thickness. The the amplification factor f, was added to artificially increase the growth, as originally the growth simulated was negligible. With $f = 4.0$ the growth was comparable to other studies, see chapter 4.

$$l_2 = 2\Delta l_{max} \tag{2.20}$$

The parameter values used for the growth model can be found in Table 2.4 below.

Table 2.4: An overview of the parameter values used for the growth algorithm.

Parameter	Value	Unit
a	0.02	
b	0.01	
f	4.0	
l_1	0.109375	mm
Δl_{max}	2.0	mm
c_g	0.0530	

2.7.3. Spatial Smoothing

During the project, it was discovered that the used methodology was sensitive to mesh distortion, due to elements collapsing or invading other elements. In many cases nearby elements had large differences in osteogenic index, causing a large difference in growth magnitude and direction. Because of this, a spatial influence, equivalent to that used in the remodeling algorithm [38, 39], was introduced. This works as a type of spatial smoothing and was applied to both the magnitude and the direction of the growth.

$$\epsilon = c_g \left(\epsilon_b + \frac{\sum_{i=1}^{N_{GP}} f_i(x)\sigma_{Si}(x,t) + \sum_{i=1}^{N_{GP}} f_i(x)\sigma_{Hi}(x,t)}{\sum_{i=1}^{N_{GP}} f_i(x)} \right) * \sum_{i=1}^{N_{GP}} f_i(x)\mathbf{u_{g,i}}(x,t) \tag{2.21}$$

After applying the smoothing function, the growth algorithm encountered mesh distortion errors only very rarely, and it was able to complete all growth simulations for the prescribed number of growth increments.

2.7.4. Growth Algorithm

The growth algorithm consists of multiple different Python functions, that collectively read the remodeling results to obtain the required stresses in the growth plate, calculate the resulting expansion coefficients, write an Abaqus input file for the growth simulation, and one to start the growth simulation.

The function used for loading the remodeling results is used for all processes where Abaqus simulation results are needed. It searches the .dat-file created by the simulation for the desired information, in this case the stress components. In the .dat-file these can be found by by a string containing ”S11”, ”S12”, et cetera. The program reads all values for these stress components, and passes those to the next function.

The next function uses information on the mesh, from the global memory; the stresses; and the growth parameters to first calculate the growth factors, c_g and l_2. Next, it calculates the exponential distances between all elements in the growth plate. Then all the principal stresses and resulting σ_{Si} and σ_{Hi} are calculated, as well as the initial growth direction for every element. The function then calculates the expansion coefficients using Equation 2.21.

These expansion coefficients are then passed to the function that writes the Abaqus input file for the growth simulation. This simulation needs to have a Coupled Temperature-displacement analysis, with C3D8T elements. All non-growing bone is assigned a low Young’s modulus of 50.0 MPa, a poisson’s ratio of 0.3, heat conductivity of 0.0 $W{\cdot}m^{-1}{\cdot}K^{-1}$, heat capacity of 1.0E3 J/K, density of 1.0 g cm^{-3}, and expansion coefficients of 0.0 in all directions. For every element in the growth plate a material definition and section assignment is made. All elements in the growth plate have their orthotropic expansion coefficients defined by the previous function. Additionally, the following material properties are used: Young’s modulus of 5000.0 MPa, a poisson’s ratio of 0.49, heat conductivity of 0.0 $W{\cdot}m^{-1}{\cdot}K^{-1}$, heat capacity of 1.0E3 J/K, density of 1.0 g cm^{-3}. The expansion is performed using a boundary condition on degree of freedom number 11, which is the temperature, on all elements in the growth plate, using a temperature of 1.0. Additionally the model is fixed at the distal end, to prevent any other translation or rotation. More lines are added to instruct Abaqus to write a .dat-file with all nodal displacements. Finally, the simulation is submitted by Python to the Abaqus solver.

When the simulation has been completed, the nodal displacements are read and added to the original nodal coordinates of all nodes in the model. The model geometry is then updated, so that the model used for remodeling has the new mesh.

3

Results: Remodeling

The first chapter of the results is on the remodeling results. This chapter contains a mesh convergence study, sensitivity analysis and comparative analysis where the density distributions resulting from the the current algorithm are compared to density distributions from previous studies.

3.1. Convergence

First, the remodeling algorithm and 3D finite element model are studied to determine their behaviour for different element sizes. Both the remodeling algorithm and the growth algorithm use stress as a (part of the) mechanical stimulus used to determine the adaptation. Additionally, the remodeling algorithm also uses strain, to calculate the strain energy density.

3.1.1. Stresses

The first measure used to determine at what mesh fineness the stress has converged is three stress values in the model, at $t = 0$ seconds. This is before the remodeling algorithm start to influence the stress distribution through the bone. As can be seen in Figure 3.1, the stresses at the transition from the outer neck to the greater trochanter converge at approximately 5.0×10^4 elements. When excluding the distal region where the boundary conditions are applied, the maximum stresses are found in the inner neck region. This maximum stress also converges at the same number of elements. Lastly, the minimum stresses anywhere in the model, decreased with an increasing number of elements.

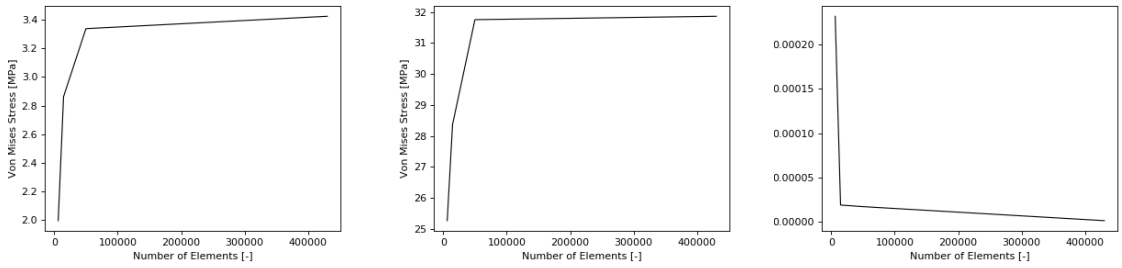

(a) (b) (c)

Figure 3.1: Different stresses for different number of elements in the model are given: a) von Mises stress at the transition between the greater trochanter and the superior neck region; b) maximum von Mises stress in the inferior neck region; and c) the minimum von Mises stress in the model, in all cases found near the greater trochanter.

3.1.2. Density distribution

Next, it is examined how the bone density distribution is affected by the mesh size. This is done visually, as well as checking both the mean and the standard deviation of the bone density distribution. The mean and standard deviation, as well as their derivatives, can be found in Figure 3.2. It is observed that at $t = 100$ the mean density is highest in the finest mesh, while the lowest mean density is observed in the least fine mesh. The standard deviation is very similar for all meshes, furthermore there is no

clear pattern of a decrease or increase in standard deviation for an increasing number of elements in the model. The closer the derivatives of the mean and standard deviation are to 0, the closer the model is to reaching remodeling convergence. Both the derivatives behave almost equally for all meshes, and are moving towards reaching convergence at a similar rate.

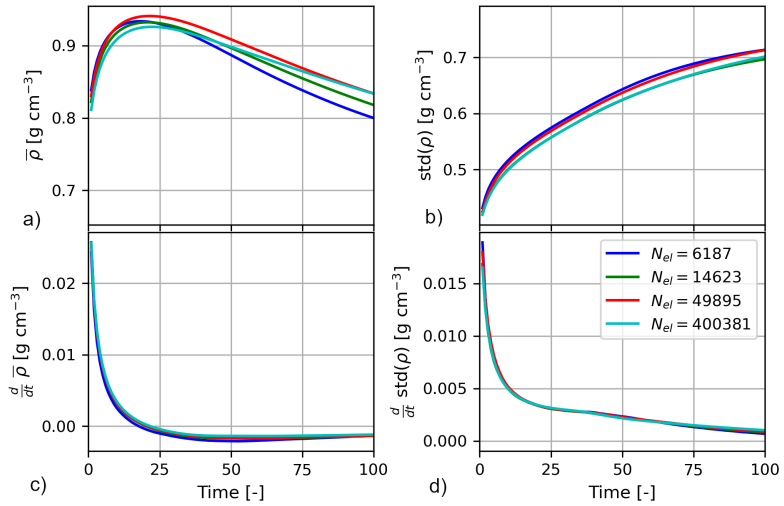

Figure 3.2: Different characteristics of the bone density for different mesh sizes. a) The mean density of the bone; b) the standard deviation of the bone density; c) change in mean density over time; and d) the change in standard deviation of the density over time.

When visually examining the outer surface of the femur, see Figure 3.4, it can be observed that high densities occur in the same regions in all models. Slight variations are expected, since the surfaces on which the loads are applied are individually applied by a human. Therefore, the exact locations and surface areas have some variance. Despite these human induced variance the density distributions present little differences between models. The most notable changes between models are the thickness and location on the hip load contact force, the gluteus maximus and the gluteus medius.

When visually examining a cross-section of the femur, see Figure 3.5, it is again observed that the density distributions are similar. In the case of the cross-section the most notable changes are the increase of details for smaller element sizes, the blocked structure in the rougher meshes and the less well defined dense bone regions in the distal lateral region. Again slight variations in the locations of certain dense bone structures can be expected, due to the human induced uncertainty on the load locations.

3.1.3. Computational time required

Lastly, it is important to analyze the required time to complete the remodeling analyses for the different meshes. If done correctly, a finer mesh should always improve the quality of the results, however it will also increase the time needed to complete the simulations. As can be seen in Figure 3.3, the time increases slightly exponentially with an increasing number of elements. As a result of this, running simulations with over 50,000 elements quickly becomes inefficient.

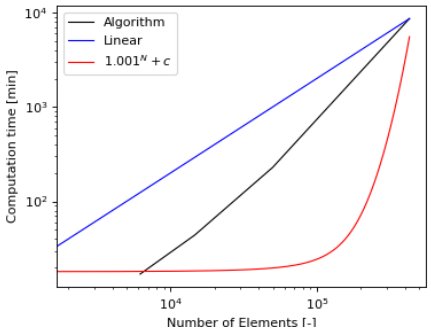

Figure 3.3: The computational time required to complete a full analysis, including the computation of the osteocyte distance function. The current algorithm (black) is compared to both a linear blue and an exponential red increase in computational time.

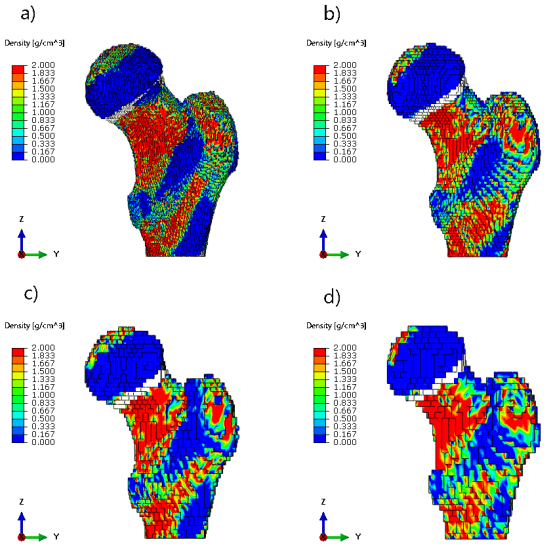

Figure 3.4: The resulting density distribution on the outer surface of the bone, for four different meshes with number of elements: a) 400381; b) 49895; c) 14623; and d) 6187

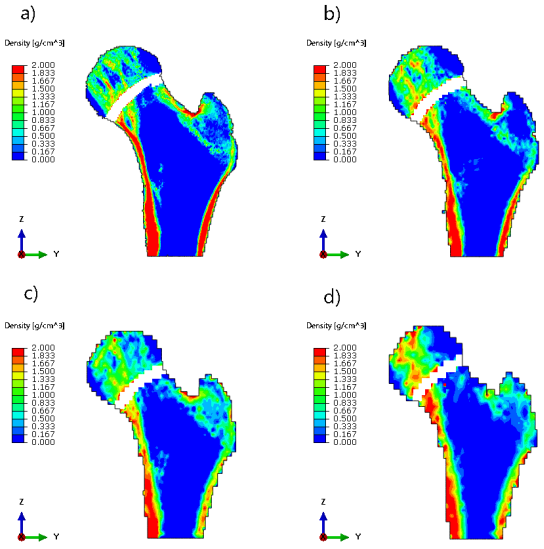

Figure 3.5: The resulting density distribution in the coronal plane of the bone, for four different meshes with number of elements: a) 400381; b) 49895; c) 14623; and d) 6187

3.2. Sensitivity analysis

In this sensitivity analysis on the remodeling parameters the effect of changes in these parameters is explored. The parameters of interest are: k, the reference constant; B, the time-constant; D, the osteocyte distance coefficient; l, the lazy-zone size; N_{incl}, the number of included nearby elements in the osteocyte weighting function; and f, a force factor multiplier.

3.2.1. k, the Reference Signal Constant

The reference signal constant, k, influences the equilibrium point of remodeling. A higher value of k will result in less dense bone, while a lower value for k results in higher densities.

As can be seen in Figure 3.6, the mean density increases with lower values for k. The standard deviation initially increases as k increases, however near a maximum of $k = 2.0 \times 10^{-4}$ J/g the STD decreases again. For low values of k much of the bone has the maximum density, with few areas of low density bone, therefore the standard deviation is low. As k increases, more low density regions start to form, increasing the STD. As k increases further, much of the high density bone starts to be converted into low density bone, decreasing the standard deviation.

Visually, it is observed in Figure 3.7 that the variance is highest around $k = 2.0 \times 10^{-4}$ J/g, with more dense bone for low values of k and more low density bone for higher values of k.

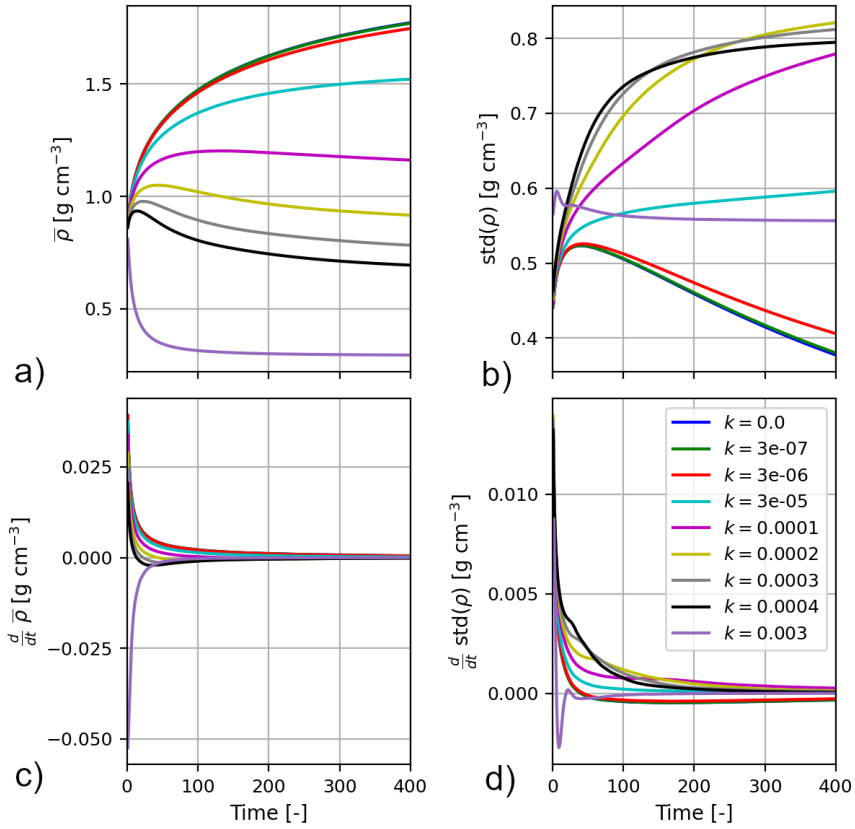

Figure 3.6: Different general measures on the apparent bone density distribution: a) the mean apparent density; b) the standard deviation of the apparent density; c) the derivative of a) the mean density; and d) the derivative of b) the standard deviation of the density. These are used to compare the sensitivity of the remodeling model to the influence of the reference $\frac{SED}{\rho}$, known as k.

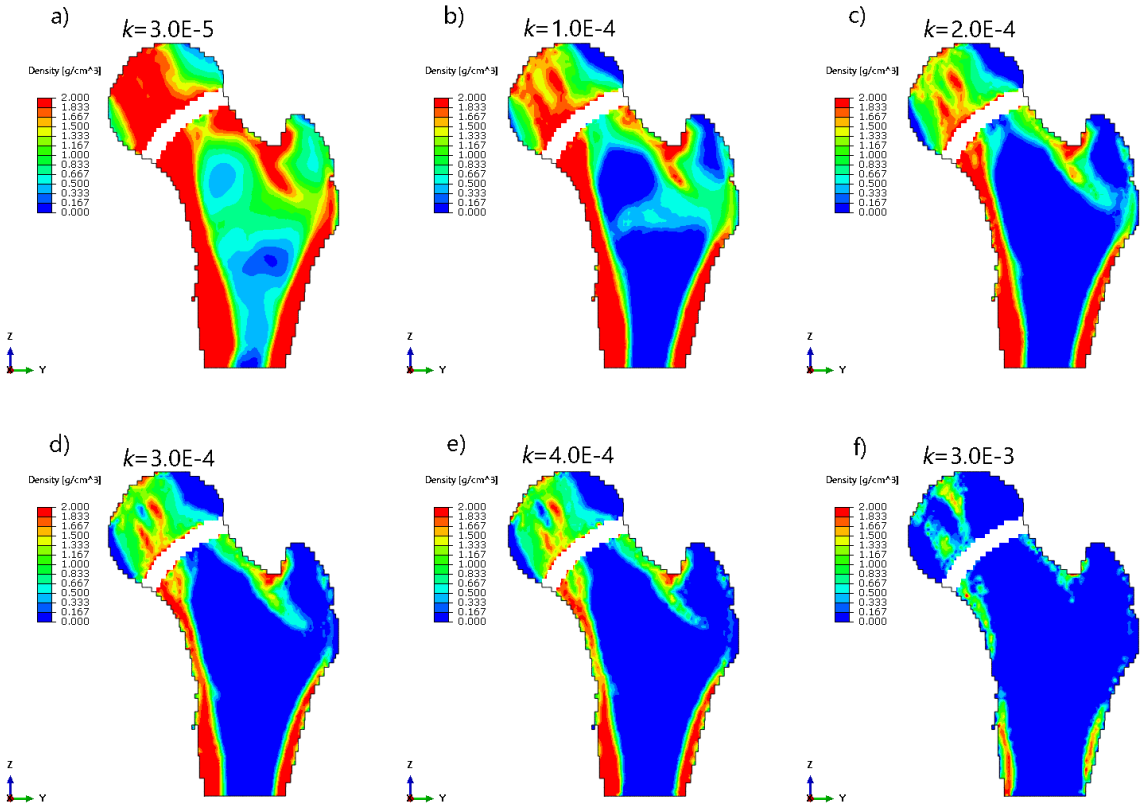

Figure 3.7: Density distributions for different values of k by increasing order.

3.2.2. B, the Time Constant

The time constant, B, influences the speed of remodeling. A higher value of B will result in faster remodeling, but when the value of B is too large instabilities are to be expected. When the value for B is too low, the simulation will take an excessive amount of time to reach the equilibrium.

As can be observed in Figure 3.8, for low values of B the model is not yet close to equilibrium after $600+$ simulation steps, while for higher values of B the algorithm clearly reaches the equilibrium faster. This can be seen by checking the convergence of both the mean and standard deviation of the bone densities over time. In general, the mean bone density first overshoots the equilibrium value, after which it decreases to the equilibrium. The B seems to have a small influence on the equilibrium mean bone density, this can be due to the propagation of small differences between the models. It can be seen that using the value of $B = 1000.0$ results in a model where the mean density at the first time point is close to the maximum bone density, however afterwards it decreases and reaches an equilibrium close to that of the other B values. Using $B = 10000.0$ resulted in an unstable model that oscillated between a very high and low mean bone density. The standard deviation continuously increases for all values of B, until the equilibrium is reached. Again, using higher values of B results in reaching the equilibrium value for the STD faster.

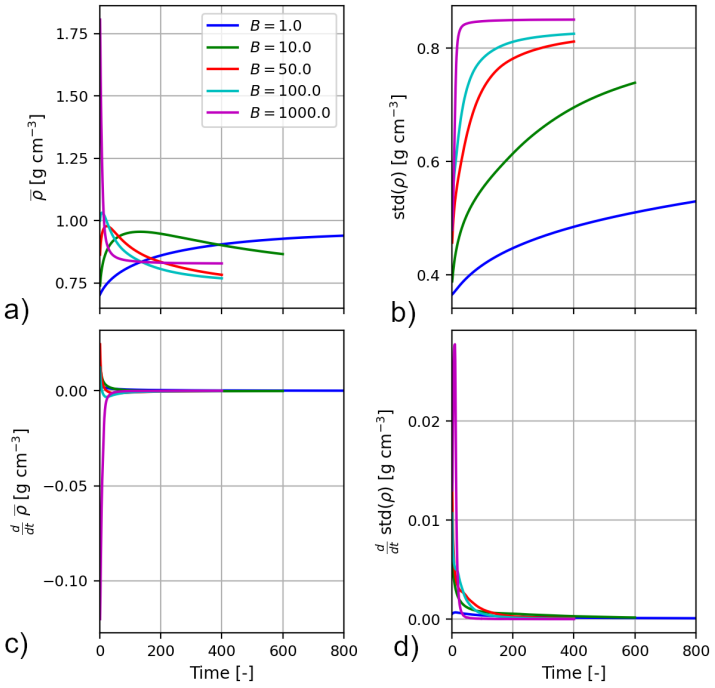

Figure 3.8: Different general measures on the apparent bone density distribution: a) the mean apparent density; b) the standard deviation of the apparent density; c) the derivative of a) the mean density; and d) the derivative of b) the standard deviation of the density. These are used to compare the sensitivity of the remodeling model to the influence of the time constant, B.

From Figure 3.9 it is clear that there are clear differences between the resulting density distributions for all values of B. One important factor in this is that these distributions were obtained at $t = 800$ for $B = 1.0$, $t = 400$ for $B = 10.0$, and $t = 400$ for the other values of B.

An interesting observation was made when using the distributions at the time where the mean bone density is at the maximum value. These distributions can be found in Figure 3.10. At this point, most density distributions are visually similar. Only when using values of $B > 100.0$ it is observed that the bone becomes excessively dense.

All models start with the density distribution obtained from the statistical shape and appearance model, and therefore the initial distributions should be close to that obtained from the remodeling algorithm. From $t = 0$ till $t = t_{\bar{\rho}_{max}}$, the cortical bone regions increase their density, while the inner parts of the bone are close to the equilibrium, and therefore do not undergo much remodeling. When the cortical bone has developed, this slowly changes and the inner density is removed along a moving line. The remodeling process can therefore be subdivided into two phases: the cortical bone development phase, and the trabecular bone removal phase.

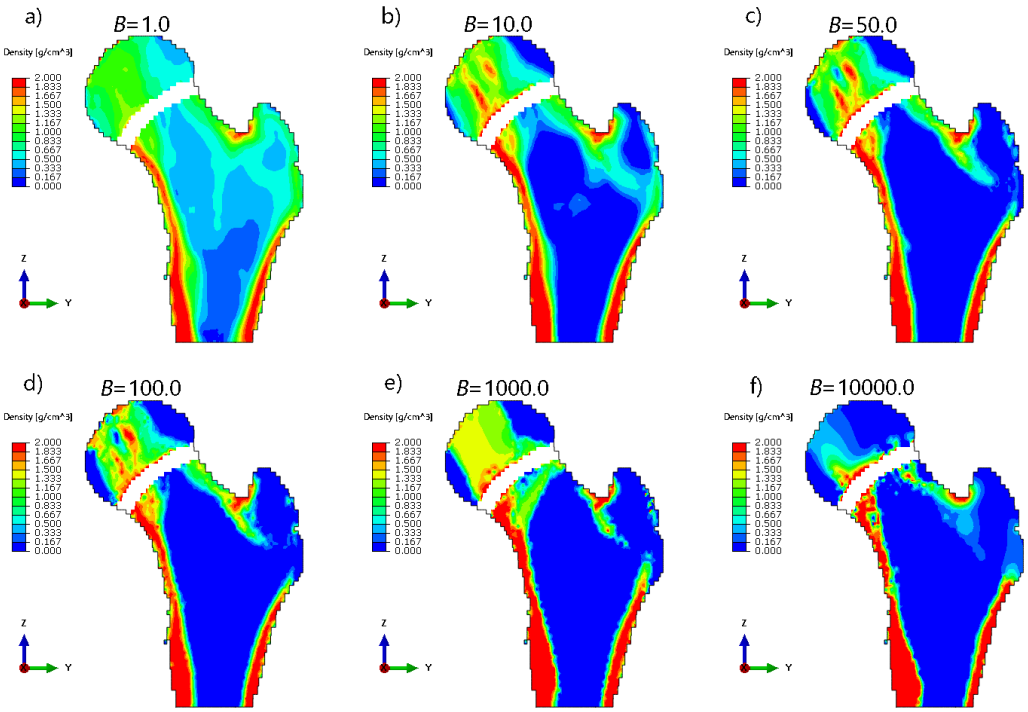

Figure 3.9: Density distributions for different values of the time constant, B, by increasing order.

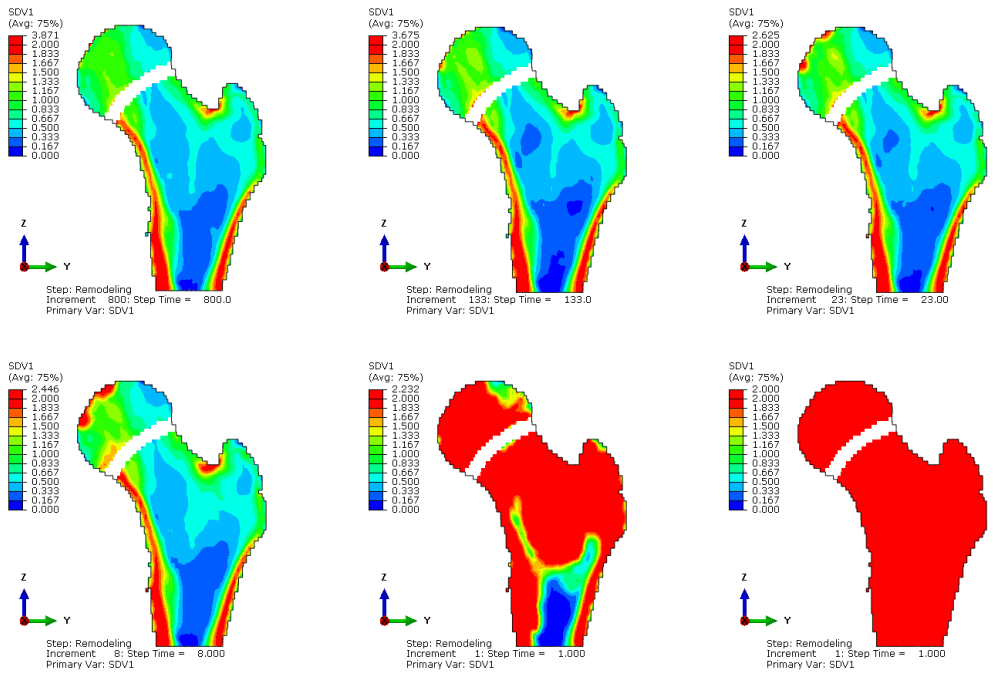

Figure 3.10: Density distributions taken at the time point where the mean of the density is at the maximum for different values of the time constant, B, in increasing order.

3.2.3. D, the Osteocyte Distance Coefficient

For the influence of nearby elements on the remodeling algorithm, D determines the rate of spatial decay. A higher value of D results in a larger area of influence. When the vale of D is too low, a checkerboard pattern is expected.

When analyzing the mean and standard deviation of the density distribution, see Figure 3.11, it is clear that the mean density increases as the distance factor is increased. However, the standard deviation remains very similar for all values of D. The derivatives of both the mean and the standard deviation show significant differences when D changes.

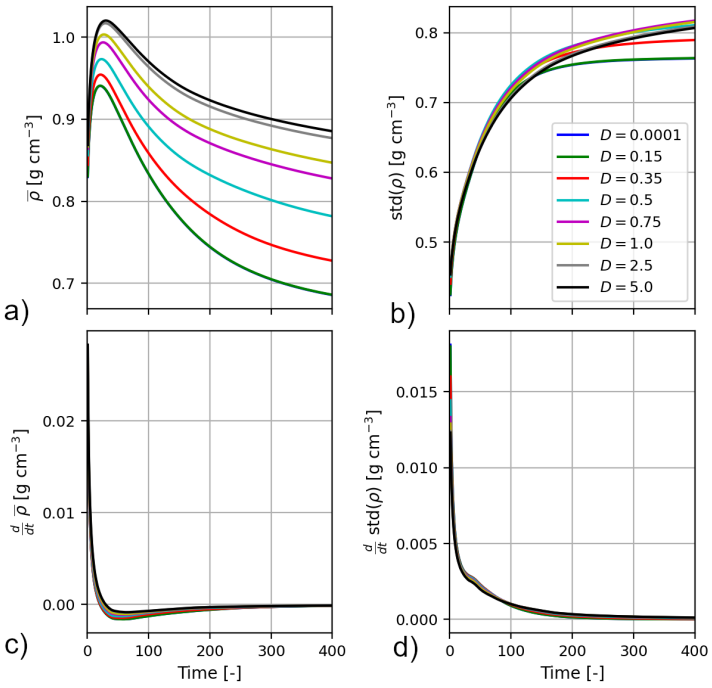

Figure 3.11: Different general measures on the apparent bone density distribution: a) the mean apparent density; b) the standard deviation of the apparent density; c) the derivative of a) the mean density; and d) the derivative of b) the standard deviation of the density. These are used to compare the sensitivity of the remodeling model to the influence of the osteocyte distance, D.

Figure 3.12 can be used to observe the differences in the density distribution in a cross section of the femur. For low values of D the distribution is not smooth and there are some regions of denser bone surrounded by regions of low density bone. For higher values the distribution is smoother, however in the femur head large regions of cortical bone develop. When compared to other studies, see 3.3, it can be seen that this not usually observed.

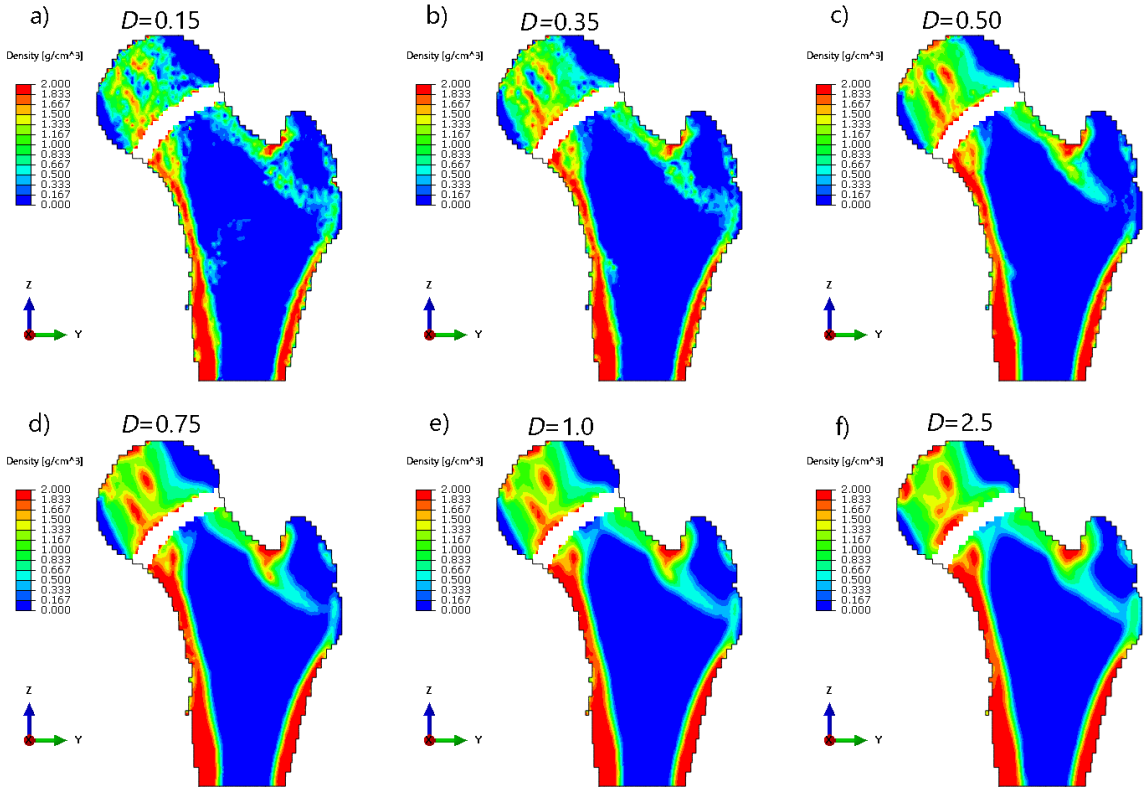

Figure 3.12: Density distributions for different values of the osteocyte distance, D, in increasing order.

3.2.4. l, the Lazy-Zone Size

The lazy zone size determines how large difference between the mechanical signal, $\Phi_i(x,t)$ and reference signal k, must be before a change in density is applied. It is expected that a larger value of l results in a simulation that converges sooner. However, elements will stop remodeling sooner, not completely reaching their equilibrium.

In Figure 3.13 it can be seen that as the lazy zone size increases the mean bone density increases, while the standard deviation is decreased. In the derivatives of both the mean and standard deviation of the bone density it is seen that for larger values of l the derivatives are closest to 0 at almost all times. This means less changes are happening throughout the model, therefore reaching convergence sooner.

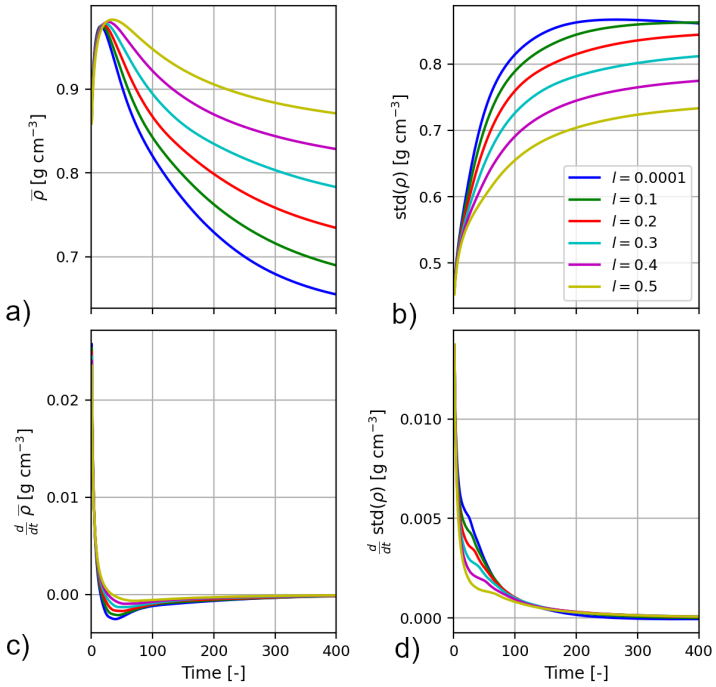

Figure 3.13: Different general measures on the apparent bone density distribution: a) the mean apparent density; b) the standard deviation of the apparent density; c) the derivative of a) the mean density; and d) the derivative of b) the standard deviation of the density. These are used to compare the sensitivity of the remodeling model to the influence of the lazy zone, l.

In Figure 3.14, it can be seen that for $0.00 \leq l \leq 0.10$ too much remodeling occurs. In the femur head the low density and high density regions are too close to each other, and the structures are relatively small. For $l = 0.50$, in the center of the cross-section there is still bone, which is unexpected and should be remodeled more. However, as can be seen in Figure 3.13, it can be seen that for this value of l the model has almost reached convergence. Therefore, it is not expected that this structure will be removed when prolonging the simulation time.

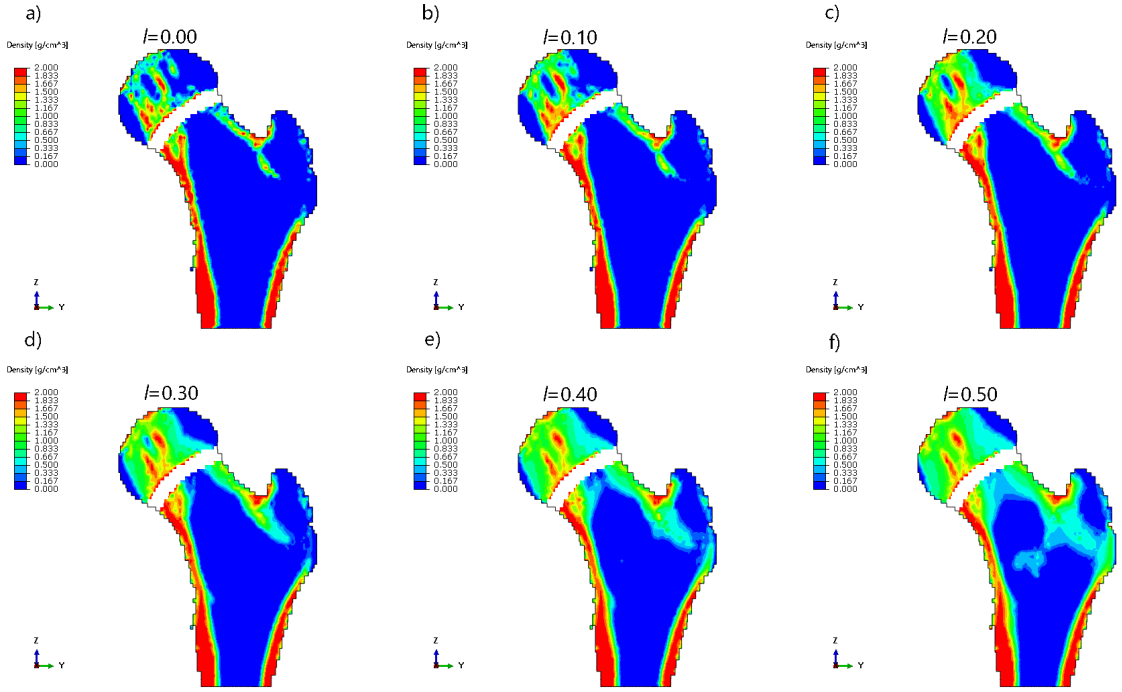

Figure 3.14: Density distributions for different values of the lazy zone size, l, in increasing order.

3.2.5. N_{incl}, the Number of Included Nearby Elements

The number of included elements in the osteocyte function should be sufficient to describe the nearby loading environment, however since the further away elements have little influence, these should have a small influence. Increasing N_{incl} yields diminishing returns, while the required computational power required increases. From Figure 3.15 it is clear that there is negligible change in the convergence rates and the standard deviation of the density distribution. There is a small change in the mean densities, where higher values of N result in slightly increased mean densities.

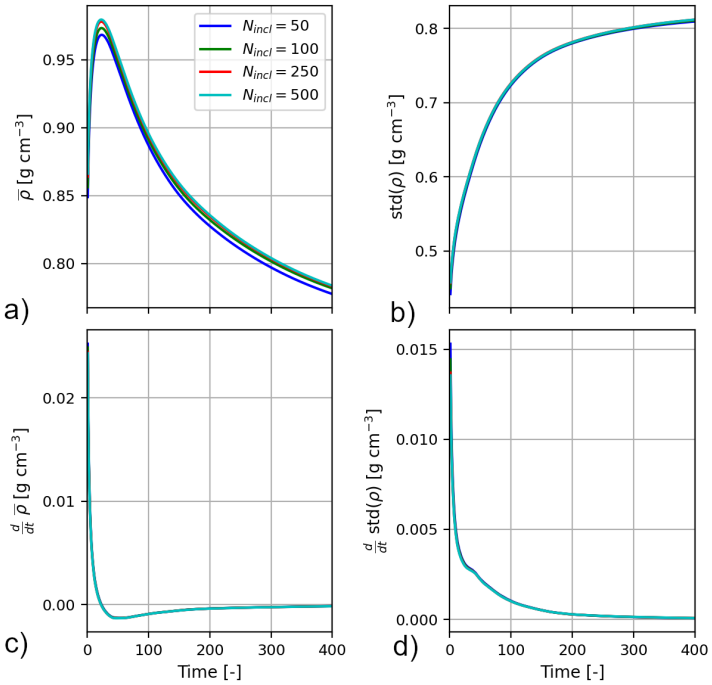

Figure 3.15: Different general measures on the apparent bone density distribution: a) the mean apparent density; b) the standard deviation of the apparent density; c) the derivative of a) the mean density; and d) the derivative of b) the standard deviation of the density. These are used to compare the sensitivity of the remodeling model to the influence of the number of nearby elements included in the osteocyte distance function, N_incl.

In Figure 3.16, it can be observed that visually there are no noticeable differences when comparing the density distributions. It can therefore be concluded that $N = 50$ is a sufficiently large amount of nearby elements, because the mean of the density shows a small difference, the standard deviation and convergence rates show no significant change and visually no differences are visible. In that case the smallest value for N is chosen for optimal numerical efficiency.

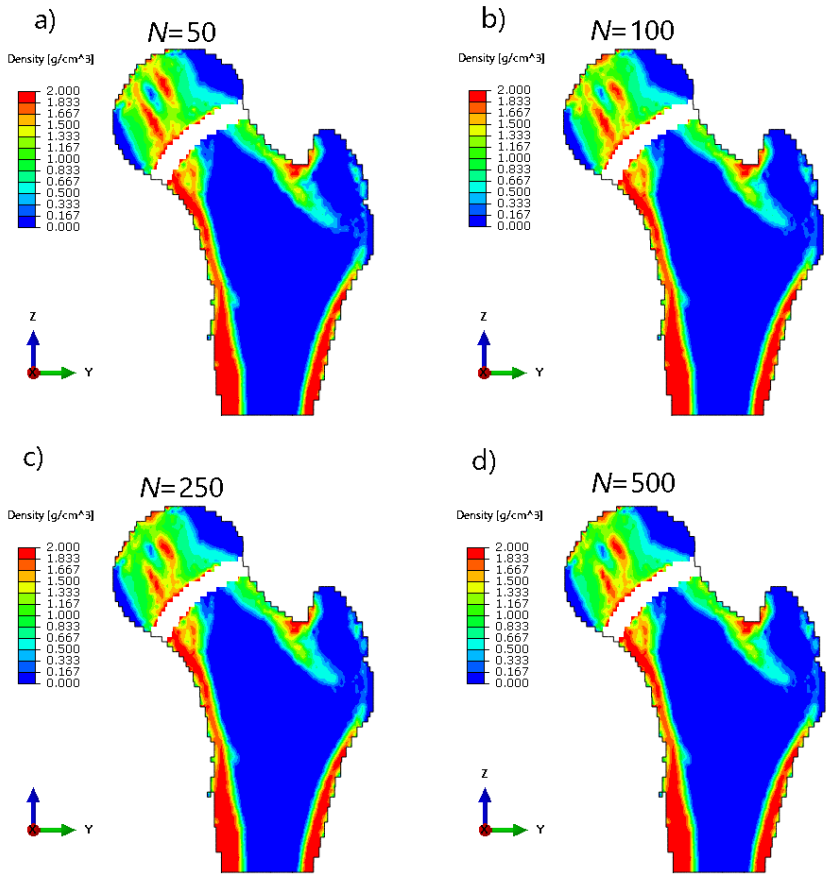

Figure 3.16: Density distributions for different values of the number of nearby elements included in the osteocyte distance function, N_incl, in increasing order.

3.2.6. f, force multiplication factor

This is a factor by which all forces are multiplied. It is not directly a component of the remodeling algorithm, however the remodeling algorithm should respond correctly to different load magnitudes. Since the increased loads should increase both the stress magnitudes as well as the strain magnitudes, the average density is expected to increase as well. In Figure 3.17, it can be seen that changing the force multiplication factor, f, results in no unexpected behaviour. The mean of the density develops in a similar fashion for all values of f. The standard deviation also develops in a predictive and expected manner.

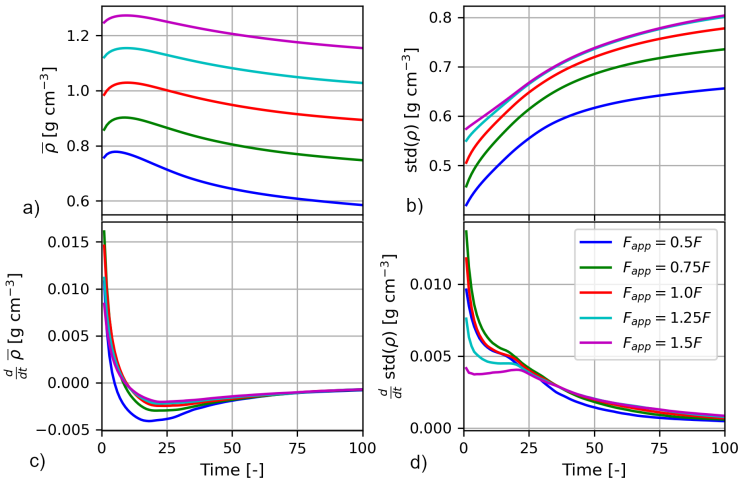

Figure 3.17: Different general measures on the apparent bone density distribution: a) the mean apparent density; b) the standard deviation of the apparent density; c) the derivative of a) the mean density; and d) the derivative of b) the standard deviation of the density. These are used to compare the sensitivity of the remodeling model to the influence of the load magnitude multiplication factor, f.

As can be seen in Figure 3.18, no unexpected behaviour appears when f is varied. The distribution generally becomes denser when f is increased. In the center of the neck and centre of bone more dense bone starts to appear as well.

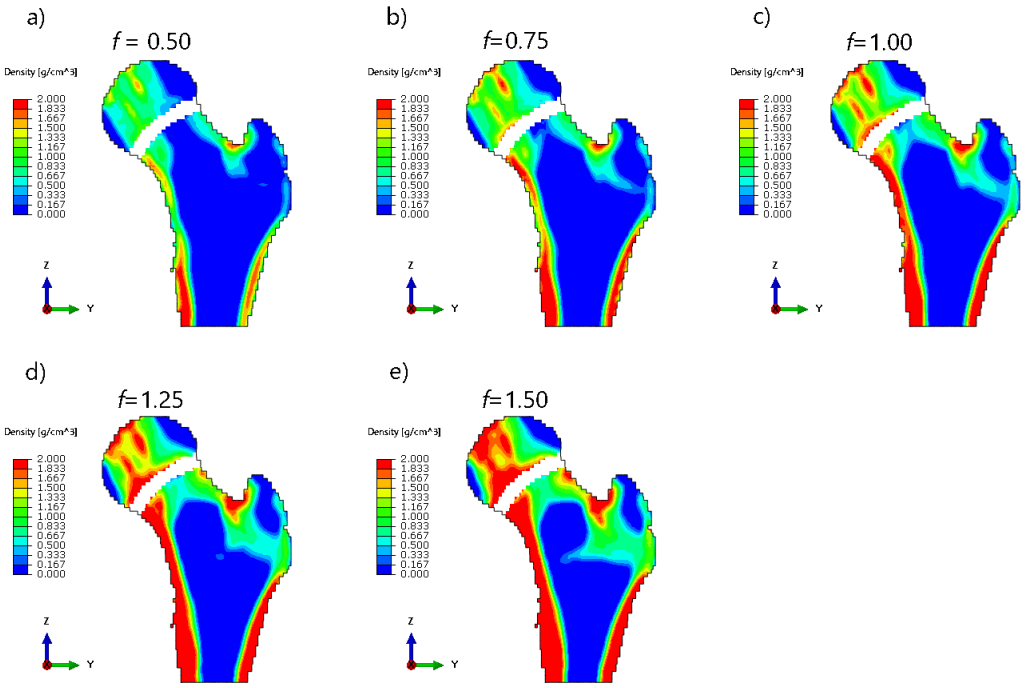

Figure 3.18: Density distributions for different values of the load magnitude multiplication factor, f, in increasing order.

3.3. Comparative analysis

The results of the remodeling model used in this study is compared to those of many previously proposed remodeling algorithms. This comparison is done mostly visually, because the absence of density information for individual elements in previous studies. Different studies also often use different loading conditions, which can result in slightly different density distributions. Three different studies were chosen for validation of the remodeling model: Campoli et al. [24], Garijo et al. [40] and Fischer et al. [41].

3.3.1. Campoli et al.

The developed remodeling algorithm is first compared to that of Campoli et al. [24]. It uses the maximum principal strain as the remodeling stimulus and uses the same loading conditions. Figure 3.19 contains the density distributions of both the study performed by Campoli et al. [24] and the density distribution resulting from this study. Compared to the resulting bone density distribution of Campoli et al. [24], the new remodeling algorithm has more cortical bone in the medial distal shell, while having less in the lateral distal shell. The density in the femur head has a higher maximum and a lower minimum. With the used density distribution many patterns of the distribution are not visible. However the main distinctions between cortical and trabecular bone are similarly positioned, with only Campoli et al. [24] predicting more cortical bone near the greater trochanter. Additionally, Garijo et al [40] provided the bone density distribution obtained from a CT-scan. When comparing the density distribution calculated by the new algorithm to the scan, there are multiple significant differences: the inner regions of the bone are more dense in the scan, the highest density region of the scan is thinner and the bone density in the head is lower in the scan. However, the the remodeling algorithm is able to predict the correct locations of the cortical bone.

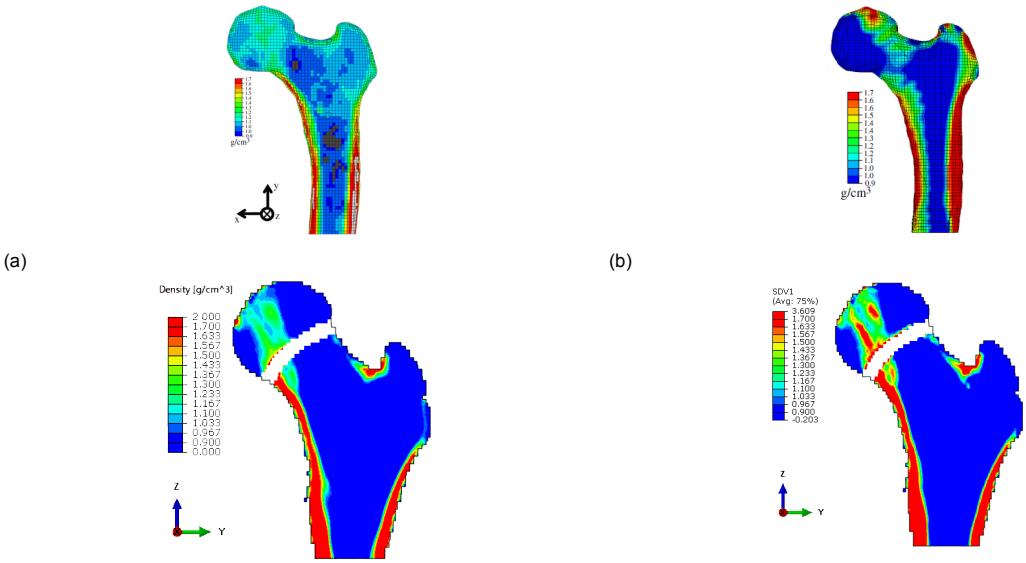

Figure 3.19: a) The density distribution obtained from a CT-scan; b) the result from the remodeling algorithm. Both modified, from Campoli et al. [24]; c) The remodeling result from the used remodeling algorithm at the increment where the mean bone density is at a maximum; and d) the resulting bone density distribution after 400 increments.

The loading conditions used in Campoli et al. [24] are similar to the ones used in the current study, as discussed in section 2.4. It is important to note the difference in shape of the proximal femur: the one used by Campoli et al. [24] has a larger greater trochanter, the neck axis angle is smaller and includes a larger region of the distal femur. It also does not include the growth plate, which has a lower stiffness than the surrounding bone.

There are two points in the development of the density distribution at which the density distribution can be compared to that of Campoli et al [24]: when the remodeling has sufficiently converged and when the mean density is at a maximum. As described in subsection 3.2.2, when the mean density is at a maximum, the cortical bone regions have been remodeled, but the trabecular regions have not

undergone much change yet. If we compare the distribution at the maximum mean density, it can be seen that the density in the head is similar to that found in Campoli et al. [24], while the rest of the density distribution remains outside the used limits for the density.

3.3.2. Garijo et al.

The remodeling algorithm used by Garijo et al. [40] uses the same minimum and maximum bone density as the developed remodeling algorithm. The remodeling method of Garijo et al. [40] uses the technique proposed by Beaupré et al. [42, 43]. Figure 3.20 contains the density distribution generated by Garijo et al [40] and those by the developed remodeling algorithm. The developed remodeling algorithm predicts similar densities in the cortical bone regions, but a lower density in the inner regions. Distal from the greater trochanter both models predict the existence of a thin region of higher density bone. In the lateral greater trochanter, Garijo et al [40] predict more dense bone than the new remodeling model. The density distribution take at time of the maximum mean bone density has a higher inner bone density, however this can be attributed to the use of the SSAM, and not to the remodeling algorithm. It however, does predict a more similar density distribution in the femur head.

The shape of the femur from Garijo et al [40] is a highly simplified 2D femur, with a smaller neck axis angle and thicker femur head. Because of the 2D model, all relevant loads are added to this slice, while the 3D model from this study has loads in different locations. A fully equivalent cross section of the 3D model is therefore not available. For example, the higher density bone at the greater trochanter is found in a different cross section of the 3D model.

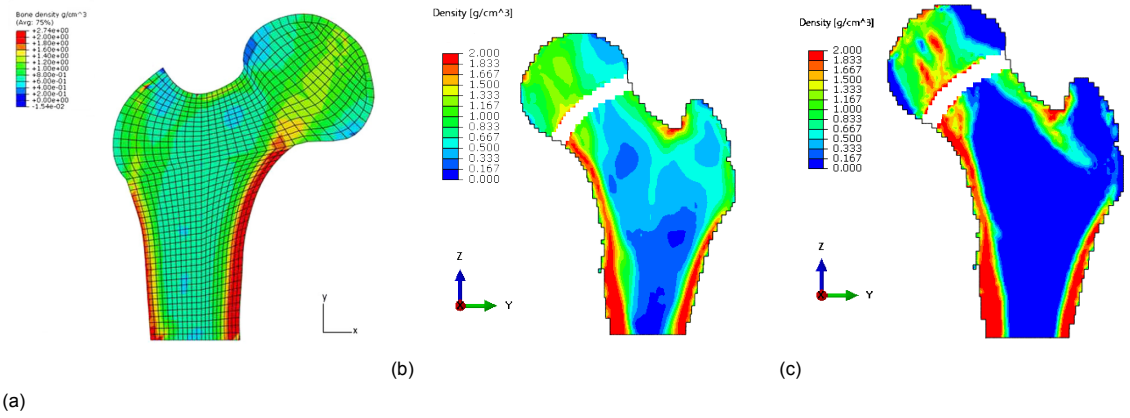

Figure 3.20: a) Result from Garijo et al. [40]; b) the density distribution at the maximum mean density; and c) the density distribution after 400 increments.

3.3.3. Fischer et al.

Fischer et al. [41] uses the same remodeling model as Garijo et al [40], which is the model by Beaupré et al [42, 43]. In Figure 3.21, when comparing the scans and simulated density distribution obtained by Fischer et al [41] to that of the current study, it is clear that the distribution predicted by the developed model is closer to the scans than the original remodeling algorithm from Fischer et al [41]. The densities in all regions except for the greater trochanter and inferior femur head are very similar. The predicted distribution by Fischer et al [41] generally predicts a density which is too low.

When using the predicted density distribution at the time where the mean density is at the maximum, the inner bone density is higher than that of the scans, however the density in the head is more similar to that of the scans, than when using the converged density distribution.

The shape of the femurs from Fischer et al [41] are obtained from QCT-scans, with a smaller neck axis angle and thicker femur head. Again a 2D model is used, due to this all relevant loads are added to this slice, while the 3D model from this study has loads in different locations. A fully equivalent cross section of the 3D model is therefore not available. For example, the higher density bone at the greater trochanter is found in a different cross section of the 3D model.

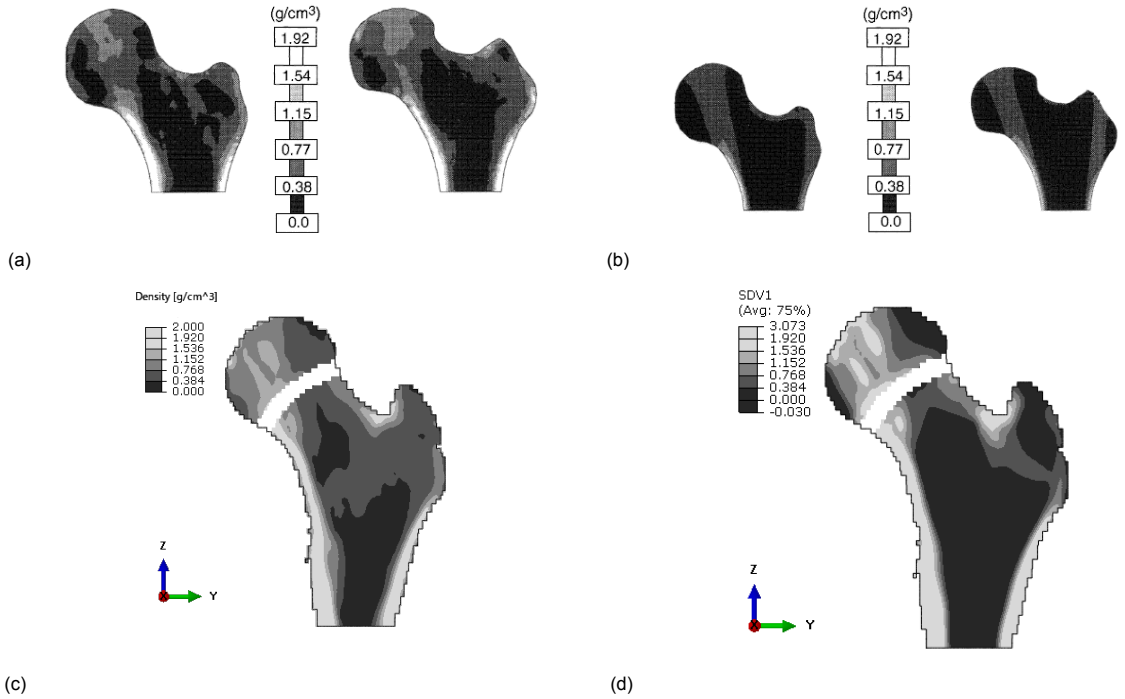

Figure 3.21: a) The density distribution obtained from a CT-scan; b) the result from the remodeling algorithm. Both modified, from Fischer et al. [41]; c) the density distribution at the maximum mean density;and d) The remodeling result from the used remodeling algorithm.

3.3.4. Conclusion

When considering all differences and similarities between the developed remodeling algorithm and those from previous studies, the following differences occur for all comparisons: the predicted bone density in the femur head is generally too high; the predicted bone density in the bone center is generally too low, the predicted bone density in the superior greater trochanter is generally too low, however this more dense bone region is found in another cross section; and the bone density around the growth plate is too high, which is partly due to the lower stiffness of the growth plate. This increases the strain, which is part of the remodeling stimulus.

Similarities found with all the three studies [24, 40, 41] are: the densities and thicknesses of cortical bone regions in the distal femur, and inner neck region; the existence of cortical bone in the outer neck region.

In general the remodeling algorithm from this study does not show extreme differences when compared to other remodeling models used for inverse remodeling models, as these show large differences when compared to each other as well.

4

Results: Growth

Different growth simulations were performed, which can be subdivided into three categories. The chapter starts with a mesh convergence study, where the effect of the mesh size on the growth is analyzed. Next is a comparative analysis, in which the results from the model created in this study is compared to results from previous studies. The third section is on a hip contact force (HCF) sensitivity analysis, which compares the resulting growth for different magnitudes of HCF. The last section is on an application of the growth model to a bone model obtained from MRI-scans from two children. The predicted growth is then compared to the growth observed in the follow-up MRI-scan. The primary measure of growth used for this study is the change in neck axis angle and when available the change in femoral anteversion.

4.1. Mesh convergence

Unfortunately, the mesh seems to have only a minor influence on the current behaviour of the growth mechanics. Realistic growth results can be achieved with both a rough and a fine mesh. However, unrealistic changes in neck axis angle can also be found. There are many factors that influence the growth behaviour, and since the growth plate is generated separately for every model, its' orientation and position vary significantly between models. Furthermore, some models distort faster than others, and mesh seems to not play a significant role in this behaviour.

The angle changes found in Table 4.1, were performed with the remodeled bone at full stiffness. It is clear that the NAA growth direction is correct, while the magnitude is a lower than expected. For the FA the direction is incorrect, but the magnitude in the right order of magnitude.

Table 4.1: Different changes in neck axis angle, NAA, and femoral anteversion, FA, for different mesh size. For these results, a non remodeling bone was used, with a constant high stiffness, corresponding to bone at 2.0 g/cm^{-3}.

Number of elements	ΔNAA [deg]	ΔFA [deg]	Steps before distortion
6187	-0.10	-0.026	9
14623	-0.13	-0.058	10
49895	-0.074	-0.0020	3

However, the goal was to create a model that would combine the internal remodeling and the longitudinal growth in the bone. Therefore, the surrounding bone should be remodeled, and have a heterogeneous stiffness. It is clear that the bone growth algorithm can achieve changes in the angle of a similar size to other studies [1, 11]. The other studies were performed using homogeneous bone stiffness surrounding the growth plate, while next the bone growth will be examined surrounding remodeled bone.

In Table 4.2, the same model is used with remodeled bone. Here it is found that the change in NAA is positive, which was negative before, as well as in other studies [1, 11]. The change in FA is much larger than expected. It is clear that the growth, when combined with remodeling does not correctly predict growth patterns, regardless of the mesh used.

Table 4.2: Different changes in neck axis angle, NAA, and femoral anteversion, FA, for different mesh size. For these results, a remodeling bone was used.

Number of elements	ΔNAA [deg]	ΔFA [deg]	Steps before distortion
14623	0.26	0.37	7
24644	0.31	0.54	9
49895	0.15	0.08	5

4.2. Comparative analysis

Next, for three shapes the change in NAA and FA are compared to values found in other studies [1, 11]. The models chosen all had around 50 thousand elements, and we therefore sufficiently converged for remodeling. The stresses in those models had also sufficiently converged.

Shape a (Res1RF2) had ΔNAA of 0.085 degrees and ΔFA of 0.0054 degrees and it completed 9 growth steps. The density distributions of this shape can be found in Figure 4.1a. The first density distribution is that after 30 remodeling steps, and the second distribution after 8 growth steps. After the final growth step, the model has been distorted, and for this reason it cannot be used again for remodeling. No significant remodeling is seen after the growth has been applied. Shape b (Res2RF1.95) had ΔNAA of 0.031 degrees and ΔFA of 0.022 degrees and it completed in 10 growth steps. The density distributions of this shape can be found in Figure 4.1b. The first density distribution is that after 30 remodeling steps, and the second distribution after 9 growth steps. For this model too, no noteworthy change in density distribution is observed.

Concluding, for all shapes, the change in NAA was in a direction that is not in accordance with other studies [1, 11]. The magnitude of ΔNAA in shapes a and b were minor, and for c large. The changes in femoral anteversion were minor in all cases and in the correct direction. The growth did not seem to have a significant impact on the remodeling after a few remodeling steps.

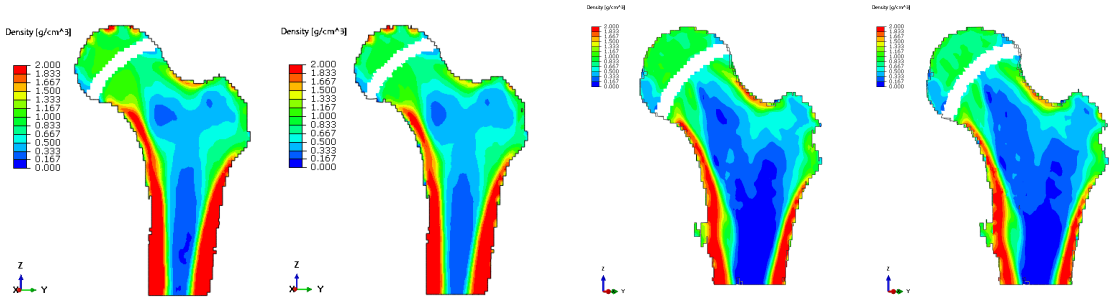

(a) (b)

Figure 4.1: The combined growth and remodeling models for different shapes, orientations and locations of the growth plate. For every shape, first the shape and appearance is shown before growth, and secondly after growth.

4.3. Hip contact force sensitivity

Different HCF magnitudes should influence both the ΔNAA and ΔFA, because the stress distribution in the growth plate changes with different HCF magnitudes. For this HCF sensitivity analysis, five different values for the HCF were used: $\mathbf{f} = [0.50, 0.75, 1.00, 1.25, 1.50]$, with

$$\mathbf{F_{HCF,i}} = f_i * \mathbf{F_{HCF}} \tag{4.1}$$

Here $\mathbf{F_{HCF}}$ is the normal hip contact force, and $\mathbf{F_{HCF,i}}$ is the applied HCF.

All other parameters are kept constant, therefore the HCF sensitivity analysis provides valuable information on the behaviour of the growth algorithm.

The results of the HCF sensitivity analysis can be found in Table 4.3. From the results, it can be concluded that little change is seen in the ΔNAA between $f = 0.50$ ($\Delta NAA = 0.014°$) and 0.75 ($\Delta NAA = 0.013°$). Between $f = 0.75$ and $f = 1.25$ the ΔNAA increases significantly with $\Delta NAA = 0.031°$

at $f = 1.00$ and $\Delta NAA = 0.053°$ at $f = 1.25$. Between $f = 1.25$ and $f = 1.50$ the ΔNAA decreases to $0.037°$.

For the change in femoral anteversion the ΔFA first increases slightly from $\Delta FA = 0.026°$ at $f = 0.50$ to $\Delta FA = 0.031°$ at $f = 0.75$. Subsequently, it decreases to $\Delta FA = 0.022°$ at $f = 1.00$. It decreases further to $\Delta FA = 0.019°$ at $f = 1.25$ and $\Delta FA = 0.012°$ at $f = 1.50$.

In conclusion, the growth algorithm is not sufficiently sensitive to the changes in the HCF. Currently, the model seems to be more sensitive to random variabilities than to the HCF. This can be because the biological growth is a much larger component of the growth than the mechanical component, however the mechanical component is already amplified using growth factor c_g.

Table 4.3: The influence of the force magnitude multiplication factor on the change in neck axis angle, ΔNAA, and the femoral anteversion, ΔFA. Additionally, the number of completed growth steps is given. All values for the change in the angles was taken after 5 steps of growth.

f	ΔNAA [deg]	ΔFA [deg]	Steps before distortion
0.5	0.014	0.026	10
0.75	0.013	0.031	10
1.00	0.031	0.022	10
1.25	0.053	0.019	8
1.50	0.037	0.012	7

4.4. MRI-scan validation

MRI-scans were obtained from two children at two different times, two years apart, resulting in four MRI-scans. This provided two possibilities for comparing the growth in a real growing bone over two years, with the growth model over five months. In order to compare the pilot scans to the follow up scans, Mimics 21.0 Research was used to obtain the NAA from 15 different slices for each scan. This was done by fitting a circle to the femur head in the coronal plane. Next, a line was drawn from the midpoint of the created circle to a point on the outer surface distal to the greater trochanter. Where the distance from the midpoint of the circle to this surface was smallest the point was placed. Next a line was drawn in the medial direction, the neck axis angle was then computed as 90 degrees plus the angle between the medial axis and the axis from the point to the center of the circle. The mean neck axis angle of all fifteen measurements was taken as the neck axis angle for that scan. This process can be observed in Figure 4.2. To determine the femoral anteversion one measures the angle between the knee axis and the femoral neck axis in the transverse plane. The angles were then compensated for the adduction in the femur, which was larger in the pilot scans. Unfortunately, the MRI-scans did not include the knee region. It was therefore decided that the MRI validation would only be performed on the change in neck axis angle.

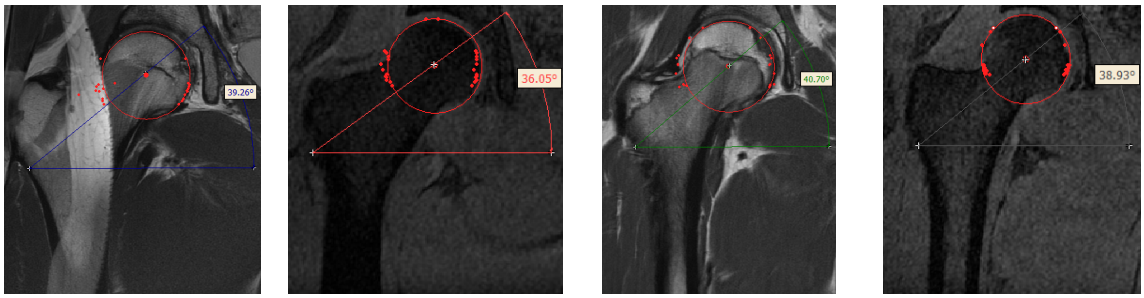

(a) (b) (c) (d)

Figure 4.2: The method used to obtain the neck axis angle, NAA, and the femoral anteversion, FA, from the MRI-scans. a) The pilot scan of patient 1; b) the follow up scan of patient 1; c) the pilot scan of patient 2; and d) the follow up scan of patient 2.

The used growth model has been developed to simulate growth for up to 5 months, however the time between the pilot MRI-scans and follow-up scans is approximately 2 years. Because of this large difference in time, they cannot be directly compared. However, the direction of growth can be compared

with that of the MRI scans. Additionally, the factor $\frac{\Delta NAA_{MRI}}{\Delta NAA_{Simulated}}$ should be similar for both patients. The comparison is based on the direction of the changes in the neck and whether the magnitude of these changes is in accordance with previous studies [1, 11]. The previous loading conditions were used again, however this time the body weight is reduced to 294.3 N, in accordance with a mass of 30 kg for $g = 9.81$ m/s^2.

For patient 1 an Abaqus model was created, which only included the HCF, as the model did not include enough details to include the muscle forces, because the scan resolution was low in the transverse plane. In the coronal plane the shape of the femur was well defined and produced a usable model. The simulated growth can be seen in Figure 4.3a. A small change in the neck axis angle is visible, however there is also a change in the shape at the greater trochanter. This is possibly due to the relatively low stiffness of the non-growing bone, a decision that was made to reduce the number of distortion errors. The change in the neck axis angle in the simulation was -0.520 degrees, while the measured change was -4.434 degrees over a two year period. For patient 2 an Abaqus model was

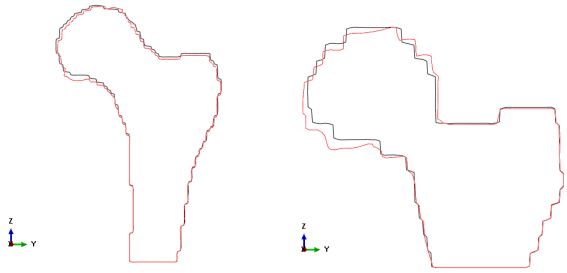

(a) (b)

Figure 4.3: The simulated growth in the models created from the pilot scans of a) patient 1 and b) patient 2. The original model is shown in black, while the grown model is shown in red.

created as well, which also only included the HCF. In the coronal plane the shape of the femur was well defined, except for the narrow neck, and produced a usable model. The quality of this model was lower than that of patient 1. The simulated growth can be seen in Figure 4.3b. Compared to patient 1 a larger change in the neck axis angle is visible. In this model, the shape of the greater trochanter and the neck remain relatively constant. The change in the neck axis angle in the simulation was -1.397 degrees, while the measured change was -5.261 degrees over a two year period.

Overall, it is clear that the magnitude of the change in the NAA is not close to that measured in the scans. However, the growth model was able to predict a larger change in NAA for patient 2 than for patient 1. It was also able to correctly predict a decrease in NAA for both patients. From Table 4.4, it can be deducted that the real growth was approximately 8.5 times larger for patient 1 and 3.8 times larger for patient 2. Unfortunately, this relative growth difference between the simulations and the scans was not similar for both patients.

Table 4.4: Changes in the neck axis angle, ΔNAA, for the simulated growth and the angles obtained from the MRI-scans.

	ΔNAA [deg] Simulated	Measured (total)	Measured (raw)	Compensation
Patient 1	-0.520	-4.434	-3.434	-1.0
Patient 2	-1.397	-5.261	-2.261	-3.0

5

Results: Influence of Bone Shape on Cam Deformity Risk

As shown by previous studies [13–18], excessive bone growth in the antero-lateral region of the growth plate can lead to the development of a cam-deformity. These cam-deformities can lead to hip osteoarthritis [14], and it is therefore important to understand what factors influence the stimulation of growth in the antero-lateral region of the growth plate. As shown by Roels et al. [13], the growth plate shape and loading conditions play a significant role in the development of cam-deformities. In this study, the influence of the bone shape is investigated.

The shapes used for this study are again created using the SSAM, where only the shape mode of interest was varied during to create new shapes. For this study the second, third and fourth mode of variation were used. From here on, these variations will be indicated using M2, M3 and M4, for Mode 2, 3 and 4. For the simulations, the previously used combined bone growth and remodeling model was used, with the same loading conditions.

5.1. Shape Variations

This section will contain a short explanation on what shape variations are used for this study. As indicated in the introduction to this chapter, these are M2, M3 and M4. Figure 5.1 contains the included variations in the shape, for every shape mode the $\mu - 3STD$, μ and $\mu + 3STD$ cases were used.

For M2, larger shape parameter values correspond with a decrease in neck-axis angle and an increase in the femoral anteversion angle. Furthermore, the femur head thickness is decreased. For M3, an increase in the shape parameter value results in a decrease in the femoral anteversion angle. The neck-axis angle and femur head thickness do not change significantly. For M4, the most significant variation is that for a lower shape parameter value the femur head is more spherical. The femur head thickness, neck-axis angle, and femoral anteversion angle remain mostly constant. Other variations in the shapes are considered not to be of significance to the growth plate mechanics.

5.2. Osteogenic Index Distribution

As mentioned in the introduction of this chapter, excessive bone growth in the antero-lateral region, also known as the cam region, of the growth plate can lead to the development of a cam-deformity. As shown by Roels et al. [13], the distribution of the osteogenic index can be used to predict the development of these cam-deformities. The values found for the osteogenic index in this chapter should be multiplied with the growth factor, c_g, with $c_g = 0.0530$.

5.2.1. Shape Variation, Mode 2

Figure 5.2 and Figure 5.3, contain the osteogenic index for the 7 different bone shapes. In Figure 5.3, the cam region can be found at the top of every growth plate. For mode 2, it can be seen in Figure 5.3, that for the $\mu - 3STD$ case the osteogenic index is highest in the cam region, which is also supported by the values found in Table 5.1. For the cases of the μ and $\mu + 3STD$ shape, the osteogenic

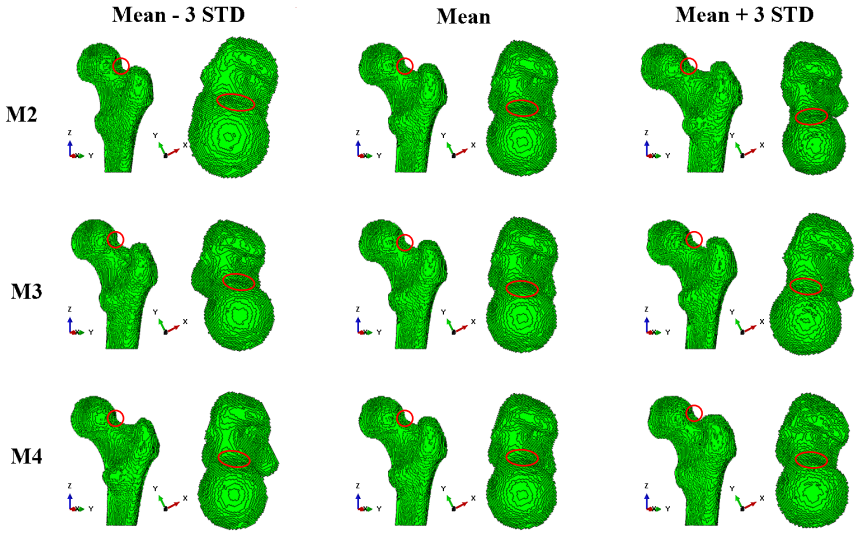

Figure 5.1: The change in shape for the second to fourth shape mode, where Mx indicates the number of the shape mode. The SSAM of Baka et al. [19, 20] was used for the creation of these models. The cam region is indicated with a red circle for the side view and oval for the top view.

index is clearly lower in the cam region, while being similar in the center. The center of the lowest osteogenic index varies a little, however this can be due to human induced differences as well.

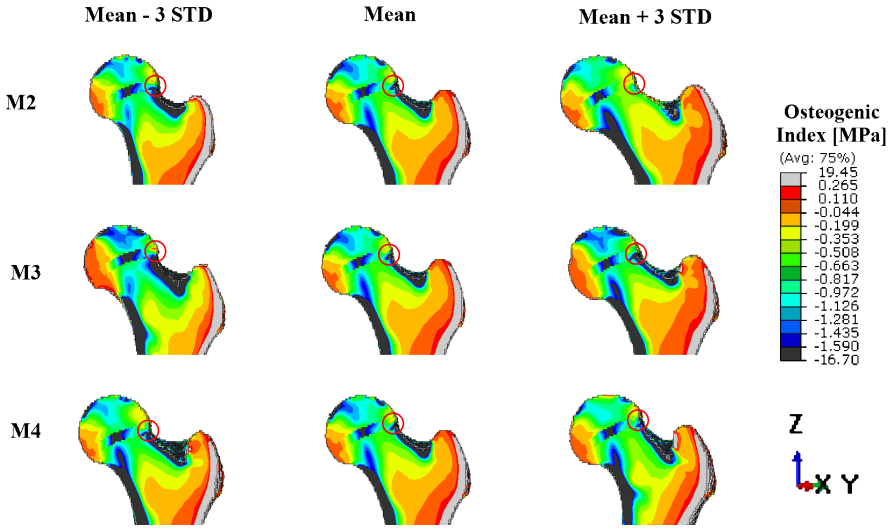

Figure 5.2: The distribution of the osteogenic index in the coronal plane for the shapes of interest. The cam region has been indicated with a red circle.

5.2.2. Shape Variation, Mode 3

For the M3 shapes, visually the osteogenic index is highest at the $\mu - 3STD$ shape, decreasing to the mean shape. It decreases further at the $\mu + 3STD$ shape. The quantitive analysis in Table 5.1 supports this analysis. The other changes can be explained by the decrease in the femoral anteversion in the bone shape, and the human factor of force surface placement.

5.2.3. Shape Variation, Mode 4

Finally for the M4 shapes, visually the differences between the osteogenic index distributions are insignificant, and can be the result of variations in human input. However, when looking at the maximum OI values found in Table 5.1, it is clear that the μ shape has the highest OI, with the $\mu - 3STD$ with

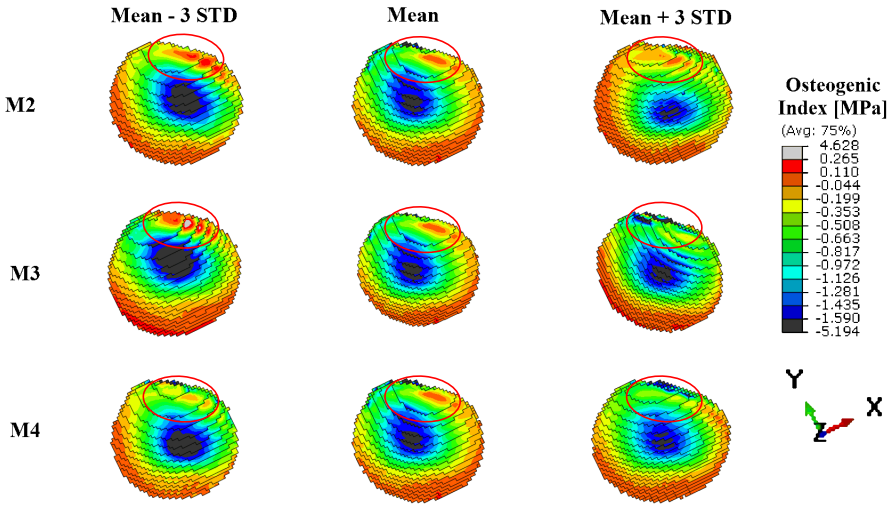

Figure 5.3: The distribution of the osteogenic index in the transverse plane, in distal direction, for the shapes of interest. The cam region has been indicated with a red oval.

the next highest OI, though much smaller. The lowest OI is that of the $\mu + 3STD$ shape. The changes in on the anterior and posterior sides of the growth plate can be caused by the human input of the placement of the loads. The minimum of the osteogenic index does not seem to move significantly between simulations.

Table 5.1: The maximum osteogenic index in the cam region for all shapes resulting from the variation in the shape modes.

Shape Mode	OI [MPa] $\mu - 3STD$	OI [MPa] μ	OI [MPa] $\mu + 3STD$
M2	0.2649	0.2031	0.1507
M3	0.4643	0.2031	−0.1109
M4	−0.01701	0.2031	0.09445

5.2.4. Simulated Growth

In addition to examining the distribution of the osteogenic index, the simulated growth can also be examined. For all shapes, 5 growth steps were simulated. The resulting changes in both the neck axis angle, ΔNAA, and the femoral anteversion, ΔFA, are shown in Table 5.2. For the changes in M2, the ΔNAA decreases as the parameter value increases, while the change in femoral anteversion shows no significant changes. For M3, the ΔNAA increases from $\mu - 3STD$ to μ, and decreases again from μ to $\mu + 3STD$. The minimum is -0.485 degrees for $\mu + 3STD$, while the maximum of -0.142 degrees if found for the mean shape. The changes in femoral anteversion are insignificant from $\mu - 3STD$ to μ, but increase significantly from μ to $\mu + 3STD$, from 0.00566 degrees to 0.489 degrees for the $\mu + 3STD$ shape. For M4, the ΔNAA decreases from $\mu - 3STD$ to $\mu + 3STD$. The minimum is -0.482 degrees for $\mu+3STD$, while the maximum of 0.131 degrees if found for the $\mu-3STD$ shape. The femoral anteversion decreases between $\mu - 3STD$ to μ, with little change for increasing shape parameter values.

Table 5.2: The simulated ΔNAA and ΔFA for the different shapes after 5 growth steps.

Type	ΔNAA [degrees]	ΔFA [degrees]
Mean	-0.142	0.00566
M2 -3STD	-0.320	-0.0103
Mean	-0.142	0.00566
M2 +STD	-0.000952	0.00119
M3 -3STD	-0.485	0.0158
Mean	-0.142	0.00566
M3 +3STD	-0.322	0.489
M4 -3STD	0.131	0.217
Mean	-0.142	0.00566
M4 +3STD	-0.482	0.0337

6

Discussion

The goal of this research was to investigate what femur shapes increase the risk of developing cam type deformities, which was done using a combined bone growth and remodeling algorithm in combination with SSAM generated femur shapes. In the Methods, chapter 2, the used methodology was presented. In chapter 3, the remodeling results of the combined bone growth and remodeling model were presented, while in chapter 4, the growth results were discussed. These previous chapters focused on the development of the combined bone growth and remodeling model. The results of the study on femur shape influence on cam type deformities were presented in chapter 5.

This chapter is subdivided into multiple sections: the combined bone growth and remodeling model is evaluated in section 6.1, while its limitations limitations are discussed in section 6.2, after which recommendations are given in section 6.3. The research on what femur shapes increase the risk of developing cam type deformities is discussed in section 6.4. The chapter ends with the conclusion in section 6.5.

6.1. Evaluation

In this section the developed combined bone growth and remodeling algorithm is evaluated. The evaluation is subdivided into four subsections: the automation, remodeling algorithm, growth algorithm and the model creation.

6.1.1. Automation

All required functions of the automation algorithm work as intended, although some functionalities could be expanded to improve the efficiency of the workflow. For example, currently the user is still required to provide certain inputs. An older SSAM algorithm has successfully been adapted to Python 3, and is able to generate 3D bone shape and appearance images. These images are then successfully converted into a 3D proximal femur model in Abaqus. Occasionally, the generated Abaqus model has a few empty elements on the interior, however this should not have a significant impact on the performance of the models. The remodeling and growth running algorithm has multiple options for choosing the type of simulation one would like to do, which work well. When one has already performed the manual inputs previously and a prepared model exists, one does not need to provide any manual input again. Also, one can choose to only perform remodeling. No such option exists for growth however, because for the current algorithm, growth is dependent on remodeling. If a simulation has previously been performed, the algorithm also provides an option to simply load the results from previous simulations.

The program is able to handle multiple different types of input and has been written in a robust way. Unfortunately, in some cases input files written by Abaqus are misread by the program. This is related to converting strings that contain numbers to a list of these numbers. The two most common problems are: when a set is created in Abaqus CAE, containing solely and all integers between to other integers (e.g. a set containing all numbers between 1 and 100) and when the Abaqus input file contains a "," as the last character in a list of numbers in a set. For the first problem, Abaqus writes the first number in the set, the last number and then the interval. So all numbers between 1 and 100 would be written as "1,100,1", but the current program reads this as if the set contains numbers 1 (2x) and 100. The

solution for this is to write a program that can recognize this pattern and read it correctly. Additionally, this function could rewrite this into a list of all integers between those numbers. A solution for the second problem is to filter out all non numerical characters (except spaces) from the list of numbers.

The program is able to correctly generate a growth plate from the locations the user provides as input. The sets created by this algorithm then have to be manually added to the old input file, an action that could be automated in future development. The algorithm properly reads the user inputs and converts them into a new input file with all required information for the simulation. The program also appends the simulation specific information to two other files, so that the simulation has all required information. The reading of results has been written in a robust manner, however it is based on repeatedly searching a large string (the data file) for certain information. This searching algorithm takes an increasing amount of time for larger models.

As will be further explained in subsection 6.1.3, the current growth algorithm does not reliably succeed at simulating realistic growth patterns. The currently build algorithm behaves correctly, however it must be adapted when implementing the recommendations made in subsection 6.3.3.

6.1.2. Remodeling

The current remodeling algorithm manages to predict realistic patterns of cortical and trabecular bone, and it manages to converge after experiencing growth steps. The chosen remodeling algorithm has a tendency to drive all values to either the maximum or minimum bone density, however these maximum and minimum values do create a well defined distinction between cortical and trabecular bone. When the remodeling algorithm is terminated before reaching convergence, the created density distribution is more realistic. The densities in the femoral head and the center of the bone are then closer to that found in other studies [24, 40, 41]. The inclusion of the osteocyte distance function significantly decreases the computational efficiency of the chosen remodeling model. However, as shown by Mullender et al [38, 39], not including the osteocyte distance function would result in a checkerboard pattern of nearby elements having either the maximum or minimum density. The inclusion of the osteocyte function in this algorithm has successfully prevented this behaviour. All other remodeling parameters have a predictable and expected effect on the behaviour of the remodeling algorithm. Multiple shapes and appearances were used for the remodeling algorithm and in all cases realistic distributions were created.

6.1.3. Growth

The growth algorithm is able to predict similar growth patterns to other studies [1, 11] in two out of three scenarios. For the unremodeled bone (section 4.1) and the MRI-scan validation (section 4.4), the growth algorithm was able to predict a correct growth direction for the NAA, although the magnitude was too small in both cases. The goal was to create a forward combined growth and remodeling algorithm based on statistical shape and appearance models. Unfortunately, for this third scenario, the algorithm failed to predict a correct direction of growth and realistic magnitudes of the change in NAA. Additionally, the combined growth and remodeling algorithm is frequently terminated before reaching the prescribed number of steps. This termination is due to distortion of the elements in the growth plate and in the surrounding elements.

Many factors are believed to influence the predicted growth: growth plate size, shape, location and orientation [11], loading conditions [10], and the mesh. In subsection 6.3.3, recommendations are given to improve the reliability and predictability of the growth algorithm.

6.1.4. Bone Model creation

The models created with the SSAM are based on 27 CT-scans of adult femurs, which was done in a previous study [19, 20]. The SSAM was created from this set of CT-scans [19, 20]. This SSAM of adult femurs, was used to generate new shapes and appearances to be used in a context where one would preferably use femurs of children. Children femurs are smaller, with a different shape, because the NAA decreases over time in healthy children [1]. For the models where these adult bone shapes were used, the growth model failed to generate realistic growth patterns, when combined with a remodeling algorithm. For the Abaqus models obtained from MRI-scans of two children, the growth algorithm performed better, and could predict the correct growth direction. For these simulations the magnitudes were also more in line with other studies [1, 11]. The changes in NAA were however much smaller than seen in the follow up scans. No significant problems were found in the creation of the

bone morphologies and corresponding meshes, and any issues in the consistency of the growth model are not believed to be caused by the bone model creation.

6.2. Limitations

The limitations of the combined bone growth and remodeling model are mostly associated with simplifications, such as linearizations or approximations. There are limitations found in the remodeling and growth algorithms, material properties, model creation.

6.2.1. Material properties

The remodeling bone in this study was modeled as a heterogeneous isotropic linearly elastic material, as done in most inverse remodeling model studies [24, 32–37, 40]. As most studies on inverse remodeling and on forward growth also used isotropic linearly elastic material properties for bone, it is believed this is not the cause of the unpredictable growth. This remodeling model focused on other mechanisms of bone adaptation and used a remodeling algorithm that is incompatible with more complex bone material models.

6.2.2. Remodeling

The first limitation in the remodeling algorithm is its dependence on only one loading scenario. Using a single loading scenario has been done in many other studies, for example in the previously mentioned inverse bone remodeling models [24, 32–37, 40, 41, 44–49], but bone actually experiences many different types of loads during everyday life. The density distributions obtained using a single loading scenario is still sufficient for the current purpose, because the distribution is realistic and mostly in accordance with other remodeling studies [24, 40, 41], as shown in section 3.3.

The second limitation in the remodeling algorithm is the use of a remodeling algorithm in which the density value of all elements eventually converges towards either the maximum or minimum density. At a macroscopic scale, bone tissue can have an apparent density at any value in between the minimum and maximum, as also shown in [24, 40]. If the current remodeling algorithm is left to fully converge it will generate an almost Boolean density distribution, which is both unrealistic and undesired. When the remodeling algorithm is terminated at an earlier stage, most of the elements will have a density at a value in between the minimum and maximum, and therefore it is advised to not let the remodeling algorithm fully converge. The density distributions obtained in this manner are more in accordance with other studies. An even better solution would be to use a different remodeling algorithm that is able to fully converge to all density values.

A third limitation of the remodeling algorithm is the lack of external remodeling. In real bone, not only the internal microstructure changes, the external shape also adapts to loads. Bone is apposed or absorbed on the outer surface, moving this surface over time. External remodeling can be a significant adaptation during growth in childhood, however its mechanisms are complex and computationally expensive. As the growth time simulated in this study was limited, it was assumed external remodeling would be minor over a small amount of time.

6.2.3. Growth

Most of the limitations associated with the growth algorithm are also mentioned in subsection 6.3.3: the simplified mesh surrounding and in the growth plate, the use of a single loading scenario, the lack of a transition zone surrounding the growth plate and the simplification of the growth plate shape. Additionally, the growth mechanics are based on a constant biological growth component and a variable mechanical growth component. This biological growth component is constant at all locations, at all times, independent of hormonal activity, age, gender, diet or other physiological factors. In reality, growth is heavily dependent on these factors [4, 50]. Despite this, previous studies have also regarded biological growth as a constant and achieved realistic growth patterns [1, 11]. The lack of physiological factors is therefore not the primary reason of the occasionally unrealistic growth patterns. Furthermore, only the growth plate in the femur head is included in the current model. Additional growth plates exist at the greater trochanter and the lesser trochanter. These may not influence the development of the NAA and FA, but inclusion of these growth plates would provide a more realistic simulation.

6.2.4. Bone model creation

All models were created using a statistical shape and appearance model, which was created using 27 CT-scans of adult femurs. These adult femurs were then used to simulate bone growth in children. However, since the neck axis angle, NAA, decreases over time, the adult bones already have a low NAA. This existing low NAA may influence the growth patterns seen when simulating the growth, as the algorithm produced more realistic results when models obtained from the femurs from children were used.

6.3. Recommendations

6.3.1. Automation

For the automated program running both the model creation, remodeling and growth a number of recommendations are made. The first is to include apparent density convergence criteria in the remodeling algorithm. An analysis is then ran until a convergence criterium is reached. An example of such a criterium is: the mean relative absolute change in density is lower than a certain percentage. Adding this to the remodeling algorithm could greatly reduce the time needed for simulations. It would also guarantee convergence regardless of the prescribed simulation time, eliminating the possibility of ending a simulation early or continuing an already converged simulation. Additionally, the surfaces used for muscle forces could be assigned automatically. One could determine the correct locations in the mean shape model of the SSAM. The location can then be transformed using the shape parameters, to find the new coordinates. Subsequently, one could find the closest outer surface in the Abaqus model to those coordinates. Furthermore, these automatically generated surfaces can also be used to automatically calculate the used surface area. This would eliminate another user input from the process. Lastly, more functions can be added to improve the visualization of growth results, one of these could be to write a separate Abaqus analysis to visualize the osteogenic index. Additionally, one could combine all deformations into a single model, where boundary conditions are applied that prescribe the deformation for all nodes. This would result in a single animation that is able to clearly visualize the growth over time. Another useful addition to the algorithm would be automatic selection of nodes that are used to calculate the NAA and FA. Currently, these nodes need to be provided as manual inputs.

6.3.2. Remodeling

The remodeling algorithm could be sped up by using a strain-based stimulus without the osteocyte distance function. In that case the model does not need to write and read both the stimulus and exponential distance values from memory for every element at every increment. As shown by Campoli et al. [24], such a model can successfully be used for the purpose of inverse remodeling algorithms.

Currently, the remodeling algorithm is only driven by one phase of gait. Even though this mostly results in the correct locations of cortical and trabecular bone, the model could benefit from including more loading scenarios, for example from [23]. For this study, only the 10% gait cycle loads are used. In this phase of the gait cycle, the hip contact force is relatively high, but the absolute maximum hip contact force occurs during another gait phase [23]. Additionally, some muscles are inactive at this gait phase, while becoming active later [23]. Taking more loading scenarios into account could improve the density distribution prediction. A downside is that this would decrease the numerical efficiency of the algorithm, as more steps and more increments will be needed.

As discussed in subsection 3.2.2, the remodeling algorithm has two states at which one can obtain the density distribution. The first state is the fully converged density distribution, which consists mostly of elements with a density of either the maximum or minimum value. This is because the remodeling algorithm drives all density values to either a maximum or minimum value. The second state is the distribution when the mean density is at a maximum. This distribution has less high density bone in the femur head, and a higher density in the center of the bone. What happens between the the density distribution at the maximum mean density and the fully converged density distribution is that in the head all elements are driven to either the maximum or the minimum value, creating a thin structure of cortical bone. These structures connect the surface where the HCF is applied to the other regions of cortical bone. Furthermore, in the center of the bone, the elements are slowly driven to the minimum density. This process is slow and computationally expensive, while providing little extra information and it decreases the validity of the density distribution. As shown by Garijo et al [40], the inner regions of

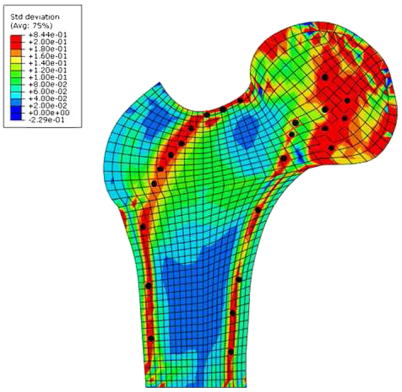

Figure 6.1

the bone vary little when the loads are changed. In Figure 6.1 it can be seen that the highest variability between simulations with different loads is found adjacent to the cortical bone regions, in the femur head and in the outer neck. All these regions have already experienced remodeling when the mean maximum density is reached, while the less important inner bone regions have not yet experienced much remodeling.

The elements surrounding the growth plate experience exaggerated remodeling. This is possibly due to the relatively low stiffness of the growth plate, which causes higher strains in the growth plate and surrounding elements. A higher strain will increase the bone density. The stiffness of the growth plate could be increased to decrease the likelihood of encountering high density bone around the growth plate. Additionally, using the density distribution when the mean density is at a maximum will further decrease the chance to encounter this behaviour.

6.3.3. Growth

Currently, the voxels are not aligned perpendicular to the growth plate. Also, instead of using layered growth, a single thicker region is expanded for every growth step. This method was chosen for easier automation, however this may have led to the current difference between the results obtained using the developed combined bone growth and remodeling model and those found in other studies, and the MRI-scans. These choices may have also led to a large amount of distortion errors when performing the growth simulations.

Another explanation for the differences between the current results and those found in other studies, is the number of loading scenarios used to determine the osteogenic index. In other studies, multiple loading scenarios from the gait cycle were used to determine the osteogenic index, while in this study only the loads at the 10% gait cycle are used. Furthermore, as suggested by Yadav et al. [11], a growth model could benefit from including additional loading patterns from different activities.

Lastly, the differences can be explained by the simplified growth plate geometry. Real growth plates come in different shapes, sizes and orientations. In this study a spherical shape was used for the growth plate, so only variance in orientation and size could be accounted for. As shown by Yadav et al. [11], both the growth plate shape and location have an effect on the osteogenic index. The resistance to growth in the model is lowest perpendicular to the growth plate, therefore most growth is performed in that direction. If the growth plate is perpendicular to the neck axis, the orientation of the growth plate is neutral. The biological growth does not promote either an increase or decrease in the NAA. However, if the growth plate is angled, such that the superior end of the growth plate is more lateral than in the neutral position, the biological growth will promote an increase in the NAA.

Another explanation for the current differences in growth is the removal of the transition zone that is seen in other studies, which was replaced by remodeling all bone surrounding the growth plate. In the femur head most stresses are transported through the center of the head towards the neck, increasing the bone density in these regions, while the more outer regions of the head are generally of low bone density. This then causes most of the stresses in the growth plate to be transported through the center. When the growth plate is placed in the neck region, the stresses are transported through the inner and outer neck, and the stresses are transported through the growth plate in a more natural position. It is therefore recommended that the growth plate is either placed in the neck region, or a transition zone is

added surrounding the growth plate, if it is placed in the femur head.

Furthermore, one could increase the stiffness of the distal remodeled bone during the growth step. In that case the distal part of the femur stays rigid, and is barely deformed, and all growth is directed towards the femoral head. The stiffness in the proximal femoral head can remain constant.

Additionally, currently the growth plate thickness is defined by the maximum distance from an element in the growth plate, to the shell of the sphere that defines the growth plate. After growth this thickness increases, but the thickness of the growth plate is not changed in the algorithm. As the expansion coefficients are dependent on the initial thickness, the simulated growth is too large. This effect is larger at the outer boundaries in radial direction, because those regions grow more rapidly than the center of the growth plate.

All these factors are believed to influence the growth in significant ways and the current results do not indicate what the core problems are. It is therefore advised to start implementing these extra mechanisms in order of increasing complexity. Firstly, one can add an algorithm that estimates the current growth plate thickness at every location. Secondly, increasing the stiffness of the distal femur during growth can be implemented. This can be done relatively easily: the algorithm needs to identify all elements distal to the growth plate and create a separate element set for this region. Next, this set needs to be assigned to a section with stiffer material properties. Thirdly, a transition zone can be added around the growth plate. This could be implemented using the same algorithm of the growth plate, with a slightly larger and smaller radius to create two extra spherical shells. These shells are proximal and distal to the growth plate, and can be assigned material properties so that the stress is distributed through the growth plate more evenly. If this does not significantly improve the reliability of the growth algorithm one can include a third simulation, in which different loading steps, associated with different time points during gait, are applied to the bone. During this third simulation bone remodeling can be turned off to increase the computational efficiency of this simulation. These forces should also improve the estimation of the osteogenic index in the growth plate. If adding more loading scenarios does not improve the simulated growth pattern either, the next suggestion is to improve the growth plate shape. One should always take care to choose the correct location, orientation and size of the growth plate, however the shape is a constant: a sphere with radius R and thickness t. The new growth plate shape could possibly be obtained from MRI- or CT-scans where the growth plate is clearly visible and thus has different gray values than the surrounding bone tissue. If changing the growth plate shape does not have the desired effect either, the last suggestion is to change the mesh in and surrounding the growth plate. This change severely affects the method of automation used for this combined growth and remodeling model and is complex to implement and even more complex to automate, and is therefore suggested last. The growth plate should be created with layers in which the elements are placed perpendicular to the growth plate. Then the layers are expanded one by one, one layer for every growth step.

6.3.4. Bone model creation

As shown by Yadav et al. [11], the growth plate shape and location have a significant effect on the osteogenic index. Therefore it would be beneficial to use a SSAM created specifically for children, which includes the variance in growth plate shape and location. In that case the growth plate region could automatically be extracted from the bone density values.

Another reason to create a SSAM based on the femurs of children, is that the NAA found in adult femurs is generally lower than those found in children, as the NAA decreases over time.

6.4. Effect of Bone Shape on Cam Deformity Development

For this study, the developed combined bone growth and remodeling model is used to investigate the effect of changing the bone shape on the development of cam type deformities in the femur. Research questions for this study were introduced in subsection 1.3.2. For this study, the created forward model was used, including material properties, loading scenarios and remodeling mechanics. The distribution of the osteogenic index in the growth plate was used to determine in which regions bone growth was stimulated, and in which regions it was inhibited. Growth stimulation in the cam-region has been linked to the development of cam-type deformities [13]. Roels et al. [13] established that the growth plate geometry and loading conditions influence the risk of cam deformity development.

The main research question is: *What femur shapes increase the risk of developing cam type defor-*

mations? With the secondary research questions being: *Of the different shape modes of the SSAM, which have a significant impact on the femur head and neck geometry? For these shape modes, what is their influence on the distribution of the osteogenic index in the growth plate? What shape modes result in an increased growth stimulation in the cam region of the growth plate?* The secondary research questions will be answered first, which will then be used to answer the main research question.

The answer to the first secondary research question will be provided first, this research question was: *Of the different shape modes of the SSAM, which have a significant impact on the femur head and neck geometry?* Three different shape modes were varied in this study and all three clearly affected the geometry of both the femur head and neck. The second shape mode (M2) greatly influences the NAA and femur head size, while also affecting the FA. The third shape mode (M3) greatly influences the FA. The fourth shape mode (M4) influences the geometry of the femur head, however it does not significantly influence the NAA and FA.

To answer the second secondary research question, the following question should be answered: *For these shape modes, what is their influence on the distribution of the osteogenic index in the growth plate?* In this study, it has been established that the bone shape also has an effect on cam deformity development. For the shape mode M2, the osteogenic index in the cam region is highest for the $\mu - 3STD$ shape. It is lower for both the μ shape and the $\mu + 3STD$ shape. For the shape mode M3, the osteogenic index in the cam region is again at a maximum for the $\mu - 3STD$ shape. The osteogenic index in the cam region is lower for the μ shape and even lower for the $\mu + 3STD$ shape. For the shape mode M4, the osteogenic index in the cam region is highest for the μ shape. It is low for both the $\mu - 3STD$ shape and the $\mu + 3STD$ shape, but at a minimum for the $\mu + 3STD$ shape.

The answers to the first and second secondary research questions can be used to answer the last secondary research question: *What shape modes result in an increased growth stimulation in the cam region of the growth plate?* From the answer to the previous research question it can be concluded that the variations in the M2 and M3 shape modes can have a significant influence on the growth stimulation in the cam region of the growth plate. For both these shape modes, the $\mu - 3STD$ shape resulted in an increase of the osteogenic index in the cam region.

The previous answers can be used to answer the main research question: *What femur shapes increase the risk of developing cam type deformations?* For the M2 and M3 shape modes, the $\mu - 3STD$ shape resulted in an increase of the osteogenic index in the cam region. Both these shapes have an increased NAA, but differ in their FA. In comparison to the μ shape: for the M2 shape mode, the FA is increased, while for the M3 shape, the FA is decreased. In conclusion, the results indicate that femurs with an increased neck-axis angle (NAA) have an increased risk of developing cam type deformations, because the osteogenic index in their cam region is increased.

6.4.1. Comparison with Carriero et al

The study of Carriero et al [1] is the first study the current results will be compared against. The primary interest is if there are differences in the methodology and differences in the resulting osteogenic index in the growth plate. Carriero et al [1] isometrically scaled down an adult proximal femur model to the size of a child. The current study did not scale down an adult proximal, instead the proximal femurs generated by the SSAM were used. The growth plate geometry of the study by Carriero et al [1] was a disc, while the current study uses a spherical growth plate shape. Carriero et al [1] subdivided the proximal femur into five different material regions, with each their own material properties. The different materials and their properties can be found in Table 6.1. The current study uses two different materials: actively remodeling bone and the growth plate. The growth plate has a slightly higher Young's modulus (6 MPa) than in Carriero et al [1]. Four load cases were used, corresponding to 10%, 30%, 45% and 60% of the gait cycle. These loads were obtained from inverse dynamics of the gait of children. The current study uses only a single load case, corresponding to 10% of the gait cycle, while the magnitude corresponds to that of an adult, because the use of an adult femur size. Carriero et al [1] calculates the osteogenic index as follows: $OI = a \times \max(\sigma_{Si}) + b \times \min(\sigma_{Hi})$, which is equal to the method used in this study when using only one load case. The values for a and b are equal in both studies: $a = 0.02$ and $b = 0.01$.

The differences in methodology, primarily femur size and loading conditions, result in a difference in the observed osteogenic index. This difference is mainly the range of values of the osteogenic index, which is $-1 \leq OI \leq +1$ for Carriero et al [1], but $-1.59 \leq OI \leq +0.265$ for the current study. The total range of both is about 2.0 for both, however the current study has much higher growth inhibition

Table 6.1: The different materials and their properties used in [1].

Region	E [MPa]	ν
Growth plate	5.0	0.49
Cortical bone	20×10^3	0.3
Trabecular bone	600	0.3
Marrow cavity	1	0.3
Transition zone	$5 - 600$	0.3

than found in Carriero et al [1]. This may be due to the differences in loading conditions: the higher hydrostatic stresses may be due to the relative increase in hip contact force in adults at 10% gait cycle. At this time point in gait, the hip contact force used for the healthy patient in Carriero et al [1] has a magnitude of 170.7% body-weight, but the current study has a hip contact force of 267.5% body-weight. Additionally, Carriero et al [1] use more load cases, which provide a more precise estimation of the osteogenic index in the growth plate.

6.4.2. Comparison with Roels et al

The study of Roels et al [13] uses the proximal femur of a 12 year old male child, obtained using a CT-scan, instead of the fully sized adult proximal femur generated by the SSAM used in this study. Both studies use a spherical growth plate, however the growth plate orientation is varied in Roels et al [13]. Both studies use the same constant material properties for the growth plate: $E = 6$ MPa and $\nu = 0.49$. The material properties of the surrounding bone are dependent on the density in both studies, however in the current study this density changes over time due to the remodeling algorithm. The Young's modulus of Roels et al [13] is determined using $E = 12900\rho^2$, while the current study distinguishes cortical and trabecular bone and generally has a lower stiffness. The poisson ratio is 0.3 for both studies. Roels et al [13] uses four load cases, but treats all as separate analyses, while the current study has a single load case. The loads of Roels et al [13] correspond: 1) the maximum hip contact force during normal gait (250% body weight), 2) internal rotation, 3) external rotation and 4) hip flexion. The load case of this study corresponds to 10% gait cycle of an adult. The osteogenic index is calculated in the same manner for both studies, however the values of a and b are different. Roels et al [13] use $b = 0.5$ and mention that $0.3 \leq \frac{b}{a} \leq 1.0$, however a value for a is not given. In most studies, $\frac{b}{a} = 0.5$, which would indicate that $a = 1$, which would explain why this value was not given. For the current study, $a = 0.02$ and $b = 0.01$, also having $\frac{b}{a} = 0.5$.

The resulting range of values for the osteogenic index in Roels et al [13] is $-0.8 \leq OI \leq +0.8$, while for the current study it is $-1.59 \leq OI \leq +0.265$. The total range is 1.6 for Roels et al [13] and 1.86 for the current study. In Roels et al [13], most cases have growth inhibition in the center of the growth plate, with growth stimulation near the edges. Again, the osteogenic index of the current study is generally lower than that found in Roels et al [13]. The primary differences between the studies are the different loading conditions and femur size.

6.4.3. Comparison with Yadav et al

In the study of Yadav et al [11], three MRI-scans of children (aged 6, 7 and 11) were used to create full femur models, compared to the proximal femurs generated by the SSAM used in the current study. The growth plates in Yadav et al [11] are subject specific, while the current study approximates the growth plate to be spherical. The material properties of the femur in Yadav et al [11] are subdivided into four materials: cortical bone, trabecular bone, transitional bone and the growth plate. Instead, the current study has two materials: the growth plate (with the same properties as in Yadav et al [11]) and the surrounding bone, which is density dependent and undergoing remodeling. Yadav et al [11] uses nine load cases corresponding to different point in time of the gait cycle, while the current study only uses a single load case, corresponding to 10% gait cycle. Yadav et al [11] calculates the osteogenic index in the same way as Carriero et al [1], however the values of a and b vary per patient. For patient 1, $a = 0.06$ and $b = 0.03$. For patient 2, $a = 0.0186$ and $b = 0.0093$. And for patient 3, $a = 0.035$ and

$b = 0.0175$. All patient have $\frac{b}{a} = 0.5$, equal to the other studies and the current study. However, the current study uses $a = 0.02$ and $b = 0.01$.

The range of osteogenic index values found in Yadav et al [11] is $-0.072 \leq OI \leq +0.072$, while for the current study it is $-1.59 \leq OI \leq +0.265$. The total range of Yadav et al [11] is therefore 0.144, while for the current study it is 1.86. This range of Yadav et al [11] is much smaller than both the current study and that of Carriero et al [1] and Roels et al [13]. This may be due to the inclusion of even more load cases than found in Carriero et al [1], but also due to the complex growth plate geometry.

6.4.4. Limitations

The developed combined bone growth and remodeling model was used for this study, and therefore the study inherits all of the limitations of the forward model. Additionally, the current study would have benefited from the inclusion of more loading scenarios and growth plate geometries. Another limitation is the use of femurs of adult size and the corresponding adult loading conditions. Additionally, the effect of more shape modes should be included to improve the understanding of the effect of the FA.

6.5. Conclusion

This research aimed to investigate the influence of the bone shape on the risk of development of camdeformities. The developed combined bone growth and internal remodeling has been automated to a large degree, and is able to predict realistic density distributions, and in certain cases growth patterns. The combined model can automatically create new bone morphologies, and the corresponding finite element models. The largest limitation of the developed combined bone growth and remodeling model is the exclusion of external remodeling, which means only the shape change in the growth plate is included. The developed bone growth and remodeling model would benefit from more automated functions, which would increase efficiency further. Additionally, some of the recommendations should be included in the growth model to improve it, so it provides more consistent and reliable results.

This developed combined bone growth and remodeling model was then used for the study to investigate the effect of a changing femur shape on the development of cam-type deformities. It was found that an increased NAA increases the bone growth stimulation in the cam-region, and therefore increases the risk of cam deformities developing. The study is limited by its use of adult sized femurs and the corresponding load conditions of adults.

In conclusion, the developed combined bone growth and remodeling model is able to provide realistic and predictable results for remodeling, and mostly for growth, and was successfully used to perform the study. This study indicates that an increased femoral neck-axis angle increases the risk of developing a cam deformation.

Bibliography

[1] Alessandra Carriero, Ilse Jonkers, and Sandra J. Shefelbine. Mechanobiological prediction of proximal femoral deformities in children with cerebral palsy. *Computer Methods in Biomechanics and Biomedical Engineering*, 14(3):253–262, March 2011. ISSN 1025-5842, 1476-8259. doi: 10.1080/10255841003682505. URL http://www.tandfonline.com/doi/abs/10.1080/10255841003682505.

[2] Gerald Jerry Tortora and Bryan Derrickson. The Skeletal System: Bone Tissue. In *Principles of Anatomy & Physiology*, pages 169–191. Wiley, 14th edition edition, 2014. ISBN 978-1-118-34500-9.

[3] Teresita Bellido, Lilian I. Plotkin, and Angela Bruzzaniti. Bone Cells. In *Basic and Applied Bone Biology*, pages 37–55. Elsevier, 2019. ISBN 978-0-12-813259-3. doi: 10.1016/B978-0-12-813259-3.00003-8. URL https://linkinghub.elsevier.com/retrieve/pii/B9780128132593000038.

[4] Matthew R. Allen and David B. Burr. Bone Growth, Modeling, and Remodeling. In *Basic and Applied Bone Biology*, pages 85–100. Elsevier, 2019. ISBN 978-0-12-813259-3. doi: 10.1016/B978-0-12-813259-3.00005-1. URL https://linkinghub.elsevier.com/retrieve/pii/B9780128132593000051.

[5] Julius Wolff. Ueber die innere Architectur der Knochen und ihre Bedeutung für die Frage vom Knochenwachsthum. *Archiv für pathologische Anatomie und Physiologie und für klinische Medicin*, 50(3):389–450, June 1870. ISSN 1432-2307. doi: 10.1007/BF01944490. URL https://doi.org/10.1007/BF01944490.

[6] Jawed A. Siddiqui and Nicola C. Partridge. Physiological bone remodeling: Systemic regulation and growth factor involvement. *Physiology*, 31(3):233–245, 2016. doi: 10.1152/physiol.00061.2014. URL https://doi.org/10.1152/physiol.00061.2014. PMID: 27053737.

[7] Dennis R. Carter and Marcy Wong. Mechanical stresses and endochondral ossification in the chondroepiphysis. *Journal of Orthopaedic Research*, 6(1):148–154, January 1988. ISSN 0736-0266, 1554-527X. doi: 10.1002/jor.1100060120. URL http://doi.wiley.com/10.1002/jor.1100060120.

[8] M. Wong and D. R. Carter. Mechanical stress and morphogenetic endochondral ossification of the sternum. *JBJS*, 70(7):992–1000, August 1988. ISSN 0021-9355. URL https://journals.lww.com/jbjsjournal/Abstract/1988/70070/Mechanical_stress_and_morphogenetic_endochondral.6.aspx.

[9] Marcy Wong and DR. Carter. A theoretical model of endochondral ossification and bone architectural construction in long bone ontogeny. *Anatomy and Embryology*, 181(6):523–532, 1990. ISSN 0340-2061, 1432-0568. doi: 10.1007/BF00174625.

[10] Sheila S. Stevens, Gary S. Beaupré, and Dennis R. Carter. Computer model of endochondral growth and ossification in long bones: Biological and mechanobiological influences: Model of endochondral growth and ossification. *Journal of Orthopaedic Research*, 17(5):646–653, September 1999. ISSN 07360266. doi: 10.1002/jor.1100170505. URL http://doi.wiley.com/10.1002/jor.1100170505.

[11] Priti Yadav, Sandra J. Shefelbine, and Elena M. Gutierrez-Farewik. Effect of growth plate geometry and growth direction on prediction of proximal femoral morphology. *Journal of Biomechanics*, 49(9):1613–1619, June 2016. ISSN 0021-9290. doi: 10.1016/j.jbiomech.2016.03.039. URL http://www.sciencedirect.com/science/article/pii/S0021929016303736.

[12] Nazli Sarkalkan, Harrie Weinans, and Amir A. Zadpoor. Statistical shape and appearance models of bones. *Bone*, 60:129–140, March 2014. ISSN 87563282. doi: 10.1016/j.bone.2013.12.006. URL https://linkinghub.elsevier.com/retrieve/pii/S8756328213004948.

[13] P. Roels, R. Agricola, E.H. Oei, H. Weinans, G. Campoli, and A.A. Zadpoor. Mechanical factors explain development of cam-type deformity. *Osteoarthritis and Cartilage*, 22(12):2074–2082, December 2014. ISSN 10634584. doi: 10.1016/j.joca.2014.09.011. URL https://linkinghub.elsevier.com/retrieve/pii/S1063458414012576.

[14] Rintje Agricola, Marinus P. Heijboer, Sita M. A. Bierma-Zeinstra, Jan A. N. Verhaar, Harrie Weinans, and Jan H. Waarsing. Cam impingement causes osteoarthritis of the hip: a nationwide prospective cohort study (CHECK). *Annals of the Rheumatic Diseases*, 72(6):918–923, June 2013. ISSN 0003-4967, 1468-2060. doi: 10.1136/annrheumdis-2012-201643. URL https://ard.bmj.com/content/72/6/918. Publisher: BMJ Publishing Group Ltd Section: Clinical and epidemiological research.

[15] K. Ito, M.-A. Minka-II, M. Leunig, S. Werlen, and R. Ganz. Femoroacetabular impingement and the cam-effect. *The Journal of Bone and Joint Surgery. British volume*, 83-B(2):171–176, March 2001. ISSN 0301-620X. doi: 10.1302/0301-620X.83B2.0830171. URL https://online.boneandjoint.org.uk/doi/abs/10.1302/0301-620x.83b2.0830171. Publisher: The British Editorial Society of Bone & Joint Surgery.

[16] R. Agricola, J. H. Waarsing, G. E. Thomas, A. J. Carr, M. Reijman, S. M. A. Bierma-Zeinstra, S. Glyn-Jones, H. Weinans, and N. K. Arden. Cam impingement: defining the presence of a cam deformity by the alpha angle: Data from the CHECK cohort and Chingford cohort. *Osteoarthritis and Cartilage*, 22(2):218–225, February 2014. ISSN 1063-4584. doi: 10.1016/j.joca.2013.11.007. URL https://www.sciencedirect.com/science/article/pii/S1063458413010121.

[17] Alex S. Nicholls, Amit Kiran, Thomas C. B. Pollard, Deborah J. Hart, Charlotte P. A. Arden, Tim Spector, H. S. Gill, David W. Murray, Andrew J. Carr, and Nigel K. Arden. The association between hip morphology parameters and nineteen-year risk of end-stage osteoarthritis of the hip: A nested case–control study. *Arthritis & Rheumatism*, 63(11):3392–3400, 2011. ISSN 1529-0131. doi: 10.1002/art.30523. URL https://onlinelibrary.wiley.com/doi/abs/10.1002/art.30523. _eprint: https://onlinelibrary.wiley.com/doi/pdf/10.1002/art.30523.

[18] Michael Doherty, Philip Courtney, Sally Doherty, Wendy Jenkins, Rose A. Maciewicz, Kenneth Muir, and Weiya Zhang. Nonspherical femoral head shape (pistol grip deformity), neck shaft angle, and risk of hip osteoarthritis: A case–control study. *Arthritis & Rheumatism*, 58(10):3172–3182, 2008. ISSN 1529-0131. doi: 10.1002/art.23939. URL https://onlinelibrary.wiley.com/doi/abs/10.1002/art.23939. _eprint: https://onlinelibrary.wiley.com/doi/pdf/10.1002/art.23939.

[19] N. Baka, B. L. Kaptein, M. de Bruijne, T. van Walsum, J. E. Giphart, W. J. Niessen, and B. P. F. Lelieveldt. 2D–3D shape reconstruction of the distal femur from stereo X-ray imaging using statistical shape models. *Medical Image Analysis*, 15(6):840–850, December 2011. ISSN 1361-8415. doi: 10.1016/j.media.2011.04.001. URL https://www.sciencedirect.com/science/article/pii/S1361841511000478.

[20] N. Baka, M. de Bruijne, T. van Walsum, B. L. Kaptein, J. E. Giphart, M. Schaap, W. J. Niessen, and B. P. F. Lelieveldt. Statistical Shape Model-Based Femur Kinematics From Biplane Fluoroscopy. *IEEE Transactions on Medical Imaging*, 31(8):1573–1583, August 2012. ISSN 1558-254X. doi: 10.1109/TMI.2012.2195783. Conference Name: IEEE Transactions on Medical Imaging.

[21] Stefan Klein*, Marius Staring*, Keelin Murphy, Max A. Viergever, and Josien P.W. Pluim. elastix: a toolbox for intensity-based medical image registration. *IEEE Transactions on Medical Imaging*, 29(1):196 – 205, January 2010.

[22] Denis P Shamonin, Esther E Bron, Boudewijn P.F. Lelieveldt, Marion Smits, Stefan Klein, and Marius Staring. Fast parallel image registration on cpu and gpu for diagnostic classification of alzheimer's disease. *Frontiers in Neuroinformatics*, 7(50):1–15, January 2014.

[23] Charalampos Bitsakos, Jan Kerner, Ian Fisher, and Andrew A. Amis. The effect of muscle loading on the simulation of bone remodelling in the proximal femur. *Journal of Biomechanics*, 38(1):133–139, 2005. ISSN 0021-9290. doi: https://doi.org/10.1016/j.jbiomech.2004.03.005. URL https://www.sciencedirect.com/science/article/pii/S0021929004001435.

[24] Gianni Campoli, Harrie Weinans, and Amir Abbas Zadpoor. Computational load estimation of the femur. *Journal of the Mechanical Behavior of Biomedical Materials*, 10:108–119, June 2012. ISSN 17516161. doi: 10.1016/j.jmbbm.2012.02.011. URL https://linkinghub.elsevier.com/retrieve/pii/S1751616112000628.

[25] D.R. Carter and W. C. Hayes. The behavior of bone as a two-phase porous structure. 59A:954, 1977.

[26] Haisheng Yang, Xin Ma, and Tongtong Guo. Some factors that affect the comparison between isotropic and orthotropic inhomogeneous finite element material models of femur. *Medical Engineering & Physics*, 32(6):553–560, July 2010. ISSN 13504533. doi: 10.1016/j.medengphy.2010.01.004. URL https://linkinghub.elsevier.com/retrieve/pii/S1350453310000068.

[27] Dieter Christian Wirtz, Norbert Schiffers, Thomas Pandorf, Klaus Radermacher, Dieter Weichert, and Raimund Forst. Critical evaluation of known bone material properties to realize anisotropic FE-simulation of the proximal femur. *Journal of Biomechanics*, 33(10):1325–1330, October 2000. ISSN 0021-9290. doi: 10.1016/S0021-9290(00)00069-5. URL https://www.sciencedirect.com/science/article/pii/S0021929000000695.

[28] Vaclav Baca, Zdenek Horak, Petr Mikulenka, and Valer Dzupa. Comparison of an inhomogeneous orthotropic and isotropic material models used for FE analyses. *Medical Engineering & Physics*, 30(7):924–930, September 2008. ISSN 1350-4533. doi: 10.1016/j.medengphy.2007.12.009. URL https://www.sciencedirect.com/science/article/pii/S1350453307001932.

[29] Liang Peng, Jing Bai, Xiaoli Zeng, and Yongxin Zhou. Comparison of isotropic and orthotropic material property assignments on femoral finite element models under two loading conditions. *Medical Engineering & Physics*, 28(3):227–233, April 2006. ISSN 1350-4533. doi: 10.1016/j.medengphy.2005.06.003. URL https://www.sciencedirect.com/science/article/pii/S1350453305001359.

[30] R. Huiskes, H. Weinans, H.J. Grootenboer, M. Dalstra, B. Fudala, and T.J. Slooff. Adaptive bone-remodeling theory applied to prosthetic-design analysis. *Journal of Biomechanics*, 20(11-12):1135–1150, 1987. doi: https://doi.org/10.1016/0021-9290(87)90030-3. URL https://www.sciencedirect.com/science/article/pii/0021929087900303?via%3Dihub.

[31] Rik Huiskes, Harrie Weinans, and Bert Van Rietbergen. The Relationship Between Stress Shielding and Bone Resorption Around Total Hip Stems and the Effects of Flexible Materials:. *Clin Orthop Relat Res*, 274:124–134, January 1992. ISSN 0009-921X. doi: 10.1097/00003086-199201000-00014. URL http://journals.lww.com/00003086-199201000-00014.

[32] Amir Abbas Zadpoor, Gianni Campoli, and Harrie Weinans. Neural network prediction of load from the morphology of trabecular bone. *Applied Mathematical Modelling*, 37(7):5260–5276, April 2013. ISSN 0307904X. doi: 10.1016/j.apm.2012.10.049. URL https://linkinghub.elsevier.com/retrieve/pii/S0307904X12006543.

[33] Patrik Christen, Keita Ito, Andreia Andrade Dos Santos, Ralph Müller, and B. Van Rietbergen. Validation of a bone loading estimation algorithm for patient-specific bone remodelling simulations. *Journal of Biomechanics*, 46(5):941–948, March 2013. ISSN 00219290. doi: 10.1016/j.jbiomech.2012.12.012. URL https://linkinghub.elsevier.com/retrieve/pii/S0021929012007427.

[34] Patrik Christen, Bert Van Rietbergen, Floor M. Lambers, Ralph Müller, and Keita Ito. Bone morphology allows estimation of loading history in a murine model of bone adaptation. *Biomechanics and Modeling in Mechanobiology*, 11(3-4):483–492, 2012. ISSN 1617-7959, 1617-7940. doi: 10.1007/s10237-011-0327-x. URL http://link.springer.com/10.1007/s10237-011-0327-x.

[35] Patrik Christen, Keita Ito, Ingrid Knippels, Ralph Müller, G. Harry Van Lenthe, and Bert Van Rietbergen. Subject-specific bone loading estimation in the human distal radius. *Journal of Biomechanics*, 46(4):759–766, February 2013. ISSN 00219290. doi: 10.1016/j.jbiomech.2012.11.016. URL https://linkinghub.elsevier.com/retrieve/pii/S0021929012006689.

[36] Patrik Christen, Keita Ito, Frietson Galis, and Bert Van Rietbergen. Determination of hip-joint loading patterns of living and extinct mammals using an inverse Wolff's law approach. *Biomechanics and Modeling in Mechanobiology*, 14(2):427–432, 2014. ISSN 1617-7959, 1617-7940. doi: 10.1007/s10237-014-0602-8. URL http://link.springer.com/10.1007/s10237-014-0602-8.

[37] Alexander Synek, Christopher J. Dunmore, Tracy L. Kivell, Matthew M. Skinner, and Dieter H. Pahr. Inverse remodelling algorithm identifies habitual manual activities of primates based on metacarpal bone architecture. *Biomechanics and Modeling in Mechanobiology*, 18(2):399–410, April 2019. ISSN 1617-7959, 1617-7940. doi: 10.1007/s10237-018-1091-y. URL http://link.springer.com/10.1007/s10237-018-1091-y.

[38] M.G. Mullender, R. Huiskes, and H. Weinans. A physiological approach to the simulation of bone remodeling as a self-organizational control process. *Journal of Biomechanics*, 27(11):1389–1394, November 1994. ISSN 00219290. doi: 10.1016/0021-9290(94)90049-3. URL https://linkinghub.elsevier.com/retrieve/pii/0021929094900493.

[39] M. G. Mullender and R. Huiskes. Proposal for the regulatory mechanism of Wolff's law. *Journal of Orthopaedic Research*, 13(4):503–512, 1995. ISSN 1554-527X. doi: 10.1002/jor.1100130405. URL https://www.onlinelibrary.wiley.com/doi/abs/10.1002/jor.1100130405. _eprint: https://onlinelibrary.wiley.com/doi/pdf/10.1002/jor.1100130405.

[40] N. Garijo, J. Martínez, J.M. García-Aznar, and M.A. Pérez. Computational evaluation of different numerical tools for the prediction of proximal femur loads from bone morphology. *Computer Methods in Applied Mechanics and Engineering*, 268:437–450, January 2014. ISSN 00457825. doi: 10.1016/j.cma.2013.10.005. URL https://linkinghub.elsevier.com/retrieve/pii/S0045782513002570.

[41] Kenneth J. Fischer, Christopher R. Jacobs, Marc E. Levenston, Dianna D. Cody, and Dennis R. Carter. Bone Load Estimation for the Proximal Femur Using Single Energy Quantitative CT Data. *Computer Methods in Biomechanics and Biomedical Engineering*, 1(3):233–245, January 1998. ISSN 1025-5842. doi: 10.1080/01495739808936704. URL https://doi.org/10.1080/01495739808936704. Publisher: Taylor & Francis _eprint: https://doi.org/10.1080/01495739808936704.

[42] G. S. Beaupré, T. E. Orr, and D. R. Carter. An approach for time-dependent bone modeling and remodeling–theoretical development. *Journal of Orthopaedic Research*, 8(5):651–661, September 1990. ISSN 07360266. doi: 10.1002/jor.1100080506. URL http://doi.wiley.com/10.1002/jor.1100080506.

[43] G. S. Beaupré, T. E. Orr, and D. R. Carter. An approach for time-dependent bone modeling and remodeling—application: A preliminary remodeling simulation. *Journal of Orthopaedic Research*, 8(5):662–670, 1990. ISSN 1554-527X. doi: 10.1002/jor.1100080507. URL https://onlinelibrary.wiley.com/doi/abs/10.1002/jor.1100080507. _eprint: https://onlinelibrary.wiley.com/doi/pdf/10.1002/jor.1100080507.

[44] Kenneth J. Fischer, Christopher R. Jacobs, and Dennis R. Carter. Computational method for determination of bone and joint loads using bone density distributions. *Journal of Biomechanics*, 28(9):1127–1135, September 1995. ISSN 0021-9290. doi: 10.1016/0021-9290(94)00182-4. URL http://www.sciencedirect.com/science/article/pii/0021929094001824.

[45] Kenneth J. Fischer, Felix Eckstein, and Christoph Becker. Density-based load estimation predicts altered femoral load directions for coxa vara and coxa valga. *Journal of Musculoskeletal Research*, 03(02):83–92, June 1999. ISSN 0218-9577. doi: 10.1142/S0218957799000105. URL https://www.worldscientific.com/doi/abs/10.1142/S0218957799000105. Publisher: World Scientific Publishing Co.

[46] K J Fischer, J A Bastidas, H J Pfaeffle, and J D Towers. A Method for Estimating Relative Bone Loads from CT Data with Application to the Radius and the Ulna. 4(3&4):397–403, 2003.

[47] N. Garijo, N. Verdonschot, K. Engelborghs, J.M. García-Aznar, and M.A. Pérez. Subject-specific musculoskeletal loading of the tibia: Computational load estimation. *Journal of the Mechanical Behavior of Biomedical Materials*, 65:334–343, January 2017. ISSN 17516161. doi: 10.1016/j.jmbbm.2016.08.026. URL https://linkinghub.elsevier.com/retrieve/pii/S1751616116302867.

[48] Max A. Bona, Larry D. Martin, and Kenneth J. Fischer. Density-based load estimation using two-dimensional finite element models: a parametric study. *Computer Methods in Biomechanics and Biomedical Engineering*, 9(4):221–229, August 2006. ISSN 1025-5842, 1476-8259. doi: 10.1080/10255840600792451. URL http://www.tandfonline.com/doi/abs/10.1080/10255840600792451.

[49] Max A Bona, Larry D Martin, and Ken J Fischer. Joint Load Estimation Based On Bone Density And A Contact Model Applied To The Proximal Femur Of A Chimp. page 2, 2003.

[50] Connie M. Weaver and Munro Peacock. Skeletal Changes Across the Life Span. In *Basic and Applied Bone Biology*, pages 189–202. Elsevier, 2019. ISBN 978-0-12-813259-3. doi: 10.1016/B978-0-12-813259-3.00010-5. URL https://linkinghub.elsevier.com/retrieve/pii/B9780128132593000105.

A

User Manual

This appendix provides a user manual of how to use all scripts to guide the user from shape and appearance parameters to a working combined bone growth and remodeling simulation. The first section describes the process of creating an .mhd-file using the SSAM script. The second section then describes the process of converting this .mhd-file into a .inp-file which can be used in Abaqus. The third and final section describes the process of using the generated .inp-file for the forward growth and remodeling simulation.

A.1. Statistical Shape and Appearance Parameter Model

This manual assumes that the required packages are installed and the needed files and executables are in the correct folders. The script requires these to be in the correct locations and the locations can be found in the script as well. The used packages are os, shutil and numpy. The complete script will not be discussed here, only the parts of interest: choices that can be made and where to make the needed changes for these choices.
The SSAM requires the shape and appearance parameters as inputs, and these can be chosen separately. The following options are provided: with the parameter values normally distributed between $-3STD$ and $+3STD$; the mean shape so that the parameter values are all 0; and the final option where a single parameter index is set to a specific value. This can be expanded to provide more options, such as one where the user provides the shape or appearance matrix. Currently, the choices are presented in the command console, so the user needs minimal knowledge of the script to use it.
Once the script has run, multiple files have been created, of which only the result.raw and result.mhd files are used for the creation of the mesh and initial density distribution.

A.2. Mesh generation

For the mesh generation the *Appearance_proximal_script.py* will be used. This script requires the following packages to run: *SimpleITK*, *NumPy*, *Matplotlib* and *SciPy*.

This script requires the user to edit the variable *BaseDir* to the folder that contains the result.raw and result.mhd files. These files can be moved after the creation of these files, so this folder can be anywhere. This is also the folder that will contain the outputs generated by *Appearance_proximal_script.py*. The outputs will be *Part_prox_red_factor_x.inp*, where *x* is the reduction factor for the mesh. This reduction factor is one of the parameters that can be tuned by the user. The script can create multiple mesh roughnesses at the same time, therefore the reduction factor(s) are set using the parameter *reductions*, which is set by a NumPy array containing the desired reduction factors. Another parameter that can be tuned is the *prox_p* parameter, which sets the relative size of the proximal femur. Higher values of *prox_p* result in a relatively smaller proximal femur region, while *prox_p*=1.0 results in a fully sized femur.

The other parameters are: *DensitiesName*, which sets the name for the .txt file with the initial density information for all elements; *b0*, which is the value of the background, currently -2000.0; *incl_f*, which determines the boundary between what values are considered to be bone: all values higher than *incl_f*b0* are bone; *min_density*, which sets the minimum bone density; and *max_density*, which sets the maximum bone density. All these parameters are currently tuned, but can easily be changed to whatever is desired: the minimum and maximum densities should not influence the mesh creation. When changing *incl_f* pay attention to existence of holes in the center of the femur, these can occur when *incl_f* is too high.

If all parameters are set correctly, one only has to run the script to generate the required mesh(es). The generated files will be the *Part_prox_red_factor_x.inp* file(s) for the Abaqus compatible mesh and the *RhoIniRFx.txt* file(s) for the initial densities. These files can be moved to whatever location is desired.

A.3. Forward Growth and Remodeling

Now that the previously created files with the mesh and initial densities are placed in the correct folder, the *FullCombinedRun.py* can be used to semi-automatically add the required features to the Abaqus model and to subsequently perform the remodeling and growth simulations.

A.3.1. Prerequisites

The following packages are required for this script: *Matplotlib, NumPy, os, re, SciPy, shutil, subprocess, sys, time* and *webbrowser*.

Furthermore, the script uses the following other scripts: *Preprocessor.py*, *GP_Set_Gen_MRI*, *DAT_reader*, *Growth_input_writer*, *Remodeling_input_writer*, *Remodeling_run*, *Expansion_Calculator*, *Expansion_run*, *FortranWrite*, *command_prompt_functions* and *InputFileInfo*.

A.3.2. Parameters

The following parameters should be set to the correct values: *RF* should be set to whatever reduction factor was previously used; *GrowthPlate_Dict* should contain the correct information for the Disc Drive, BaseDir, Results Folder and Current Result Folder, resulting in a path of ”Disc Drive:/BaseDir/Results Folder/Current Result Folder/”.

One can then set the simulation parameters *NumberOfMonths* to the number of growth steps that should be performed. With *RemodelingTimePerMonth_i* being the number of remodeling iterations performed during the first remodeling step. And *RemodelingTimeGeneral* should be set to the number of remodeling iterations for subsequent remodeling steps.

Next, one can set the growth plate shape and size parameters in *gp_params*. Here the growth plate radius can be set, as well as the allowed maximum distance of growth plate elements to the shell of the growth plate sphere.

The force magnitude can be decreased by setting both *F_factor*. The standard weight used in this model is 735 N.

The growth parameters can be set in the dictionary *GrowthParameter_Dict*. Finally, the remodeling parameters can be set in the dictionary *RemodelingParameter_Dict*. In these dictionaries the keys are self-explanatory.

Lastly, the used subroutine template can be specified in *TemplatePaths*. The number of SDV’s (solution dependent variables) in the user-subroutine should be equal to the number of SDV’s specified in *RemodelingParameter_Dict*.

A.3.3. Semi-automated model preparations

This user manual will discuss what to do more elaborately, however during the use of the script it will open multiple text files that contain a summary of what to do. These do not include exactly where to place surfaces, where to place new node sets, however they will include what these node sets should be named.

Step 1

After starting the script, the first two things that will happen are: Abaqus CAE gets opened, as well as the guide *step1.txt*. In this tutorial, this guide file will be ignored, since one does not need to do any actions here.

In Abaqus CAE, one needs to close the quick menu, and right click on Models(1) in the Model Tree. Select ”Import Model”, and import the available .inp-file in the folder. This file should be named *Part_prox_red_factor_x.inp*. Once imported, inspect the proximal femur, and use the mesh editor to remove any excessive elements. Now, first one needs to add the following node sets: *HEADNECKNODES* and *GPTOPBOTTOM*. *HEADNECKNODES* should contain all nodes proximal to the estimated position of the growth plate, while *GPTOPBOTTOM* contains an indication of the growth plate position. Contrary to what the name suggests, one can select as many nodes, at all positions as desired. However, the sphere center is calculated using an optimization algorithm, and the more nodes in this set, the less efficient this optimization becomes, while barely improving the estimated position of the growth plate. The regions to select can be found in Figure A.1.

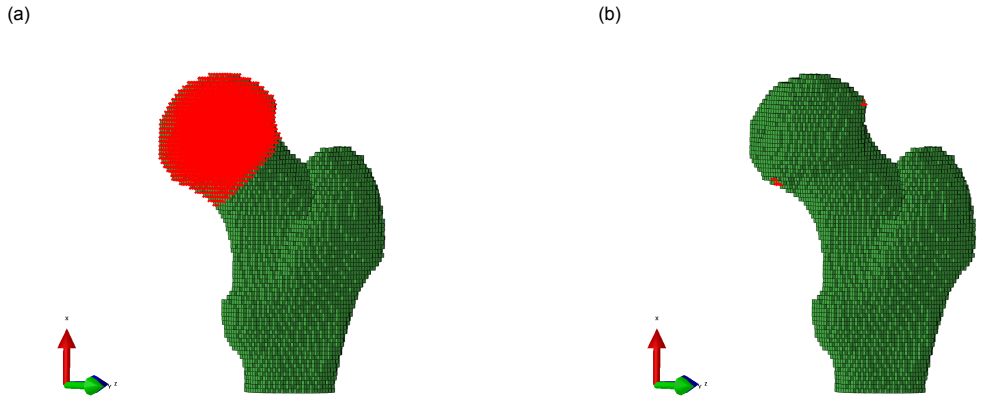

Figure A.1: The selection of two node sets is shown to indicate the locations of these sets. a) the first node set is the *HEADNECKNODES*, which contains nodes in the femoral head and where it transitions into the neck. This region will contain the growth plate, and the algorithm will restrict itself from only creating the growth plate in this region. b) The nodes selected to general position of the growth plate. The algorithm will optimize the location and orientation of the growth plate center, so that the outer surface intersects with the selected nodes. This is the node set *GPTOPBOTTOM*.

At this point, the model only contains a part, we therefore need to create an instance from this part and add it to an assembly. Next, one should create a job, called ”step1”, and perform the ”Write input” operation on this job (ignore the warning(s)), to create the file *step1.inp*. One can then close Abaqus CAE, without saving.

Step 1.5

After the previous step, the script has calculated the center of the growth plate sphere, and used this to obtain all nodes and elements in the growth plate. It has prepared a string of text that should be added to *step1.inp* to create the model with growth plate. The script will open two files, the file containing the created string and *step1.inp*. Copy the contents from the first file, and paste in a new line, right above the ASSEMBLY section of *step1.inp*. Save *step1.inp*, optionally with a different name, for example *step1_5.inp*, that way one can easily use the original *step1.inp* file and in the future one can skip the operations in Abaqus CAE for the same model.

Step 2

After saving and closing *step1_5.inp*, press Enter in the command line of Python. The script will again open Abaqus CAE, a compact tutorial file and a file that needs to be filled. During this step, the required features for the loading conditions will be added. However, the first thing to do is to check the position and orientation of the generated growth plate. If the growth plate is not oriented or positioned as desired, one should redo step 1.

Firstly, the node set called *BOTTOMNODES* will be created at the distal surface of the femur. Make sure to exclude one node in the center: if not Abaqus will write the input file as ”A, B, C”. With A being the starting number, B the last number and C the iteration size. The script however, uses ”A, B, C” as A, B and C are all numbers in the set.

Next, the loading surfaces are added to the model. The following surfaces are added: *FEMURHEADSURF, GLUTMAX, GLUTMED, GLUTMIN, PIRIFORMIS, ADDMAG, ADDMIN*. These surfaces correspond to the hip contact force, gluteus maximus, gluteus medius, gluteus minimus, piriformis, adductor magnus and adductor minimus respectively. These surfaces can be found in Figure A.2. After having done this, create a new job called ”step2” and write the input file for this job. Do not yet close Abaqus CAE.

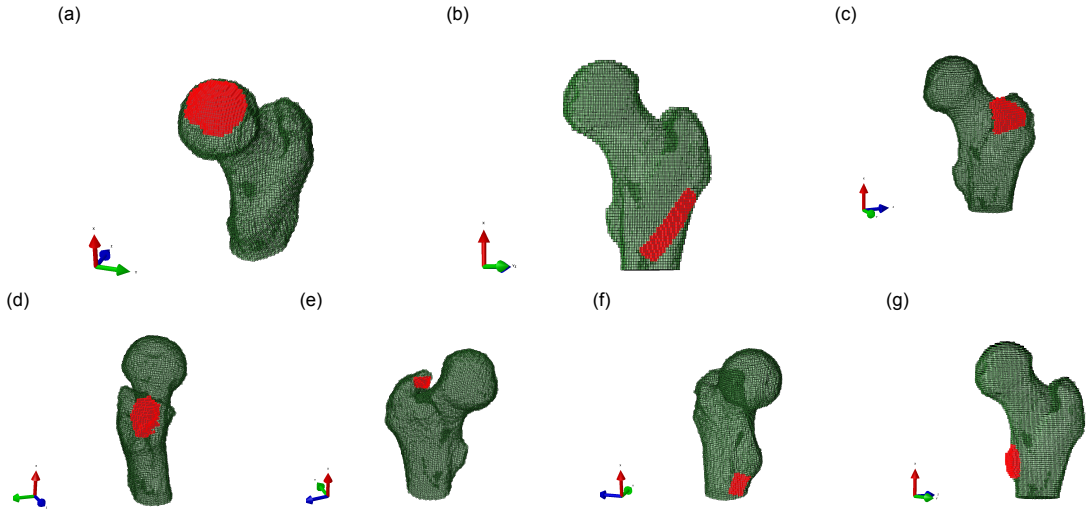

Figure A.2: The highlighted surfaces indicate the region where the surfaces should be created for the following loads: a) the hip contact force (HCF), *FEMURHEADSURF*; b) the gluteus maximus, *GLUTMAX*; c) the gluteus medius, *GLUTMED*; d) the gluteus minimus, *GLUTMIN*; e) the piriformis, *PIRIFORMIS*; f) the adductor magnus, *ADDMAG*; and g) the adductor minimus, *GLUTMIN*.

After creating these surfaces, one should use the Tools -> Query -> Mass Properties tool to obtain the surface areas of the created surfaces. One should select mesh entities in the prompt area, and then use the display manager to only display the surface of interest. Select all elements in a surface, then use the tool and the mass information is printed into the message area. The surface areas should be pasted into the *SurfArea.txt* file, line by line in the previously used order. Save and close this file. Finally, close Abaqus CAE. The script will now create the complete simulation using the provided input file. It will start both remodeling and growth simulations automatically.

B

User-subroutine

```
      MODULE Ksafe
      INTEGER,PARAMETER :: ElNum =
      INTEGER,PARAMETER :: width =
      INTEGER,PARAMETER :: icond =
      INTEGER,PARAMETER :: Svflag =

      REAL,PARAMETER :: B =
      REAL,PARAMETER :: s =
      REAL,PARAMETER :: rho_i =
      REAL,PARAMETER :: lazy =

      CHARACTER(120), PARAMETER :: ExpFileName =
     1
      CHARACTER(120), PARAMETER :: FileName2 =
     1

      REAL,PARAMETER :: a_oi = 0.02
      REAL,PARAMETER :: b_oi = 0.01

      REAL,DIMENSION(ElNum) :: Stimulus
      REAL, DIMENSION(ElNum) :: initial_statev1
      REAL,DIMENSION(ElNum,width) :: El_Exp
      INTEGER,DIMENSION(ElNum,width) :: El_Num

      ENDMODULE

      SUBROUTINE SDVINI(STATEV,COORDS,NSTATV,NCRDS,NOEL,NPT,
     1 LAYER,KSPT)
C
      USE Ksafe
      INCLUDE 'ABA_PARAM.INC'
C
      DIMENSION STATEV(NSTATV),COORDS(NCRDS)

      IF (NOEL.EQ.1) THEN
          OPEN(unit=121,file=ExpFileName)
          IF (icond.EQ.1) THEN
              OPEN(unit=105,file=FileName2)
              DO i=1,ElNum
                  READ(105,"(F)") (initial_statev1(i))
```

```
                DO j=1,width
                    READ(121,"(I,F)") (El_num(i,j), El_exp(i,j))
                ENDDO
            ENDDO
            CLOSE(105)
            CLOSE(121)
        ELSE
            DO i=1,ElNum
                DO j=1,width
                    READ(121,"(I,F)") (El_num(i,j), El_exp(i,j))
                ENDDO
            ENDDO
            CLOSE(121)
            initial_statev1(:) = rho_i
        ENDIF
      ENDIF

      !user coding to define STATEV(NSTATV)
      STATEV(1) = initial_statev1(NOEL)
      STATEV(2) = 0.0
      !STATEV(2) = 0
      !STATEV(3) = 0

      RETURN
      END

      SUBROUTINE USDFLD(FIELD,STATEV,PNEWDT,DIRECT,T,CELENT,
     1 TIME,DTIME,CMNAME,ORNAME,NFIELD,NSTATV,NOEL,NPT,LAYER,
     2 KSPT,KSTEP,KINC,NDI,NSHR,COORD,JMAC,JMATYP,MATLAYO,
     3 LACCFLA)
C
      USE Ksafe
      INCLUDE 'ABA_PARAM.INC'
C

C
      ! Initialize required variables
      REAL S11,S22,S33,S12,S13,S23,DeltaDensity,Density0,
     1 EPS11,EPS22,EPS33,EPS12,EPS13,EPS23,DeltaDensity_i
     2 Density,Young,Ua,Ub, U, gamma, invGamma, stimDiff,Stim
     3 sum_f_i,Stim_f_i,PHI,NewDensity,NewDensity_i,S_v,
     4 EPMin, EPInt, EPMax, SP1, SP2, SP3, Ssi, Shi, OI

      ! Initialize required vectors
      REAL, DIMENSION(width) :: f_i,S_i
      INTEGER, DIMENSION(width) :: num_i
C
      ! Initialize required strings
      CHARACTER*80 CMNAME,ORNAME
      CHARACTER*3  FLGRAY(15)

      ! Initialize vectors required for the CALL functions
      DIMENSION FIELD(NFIELD),STATEV(NSTATV),DIRECT(3,3),
     1 T(3,3),TIME(2)
      DIMENSION ARRAY1(15),ARRAY2(15),ARRAYSP(15),
     1 JARRAY(15),JMAC(*),JMATYP(*), COORD(*)
C
```

```
  ! Obtain strain components
  CALL GETVRM('E',ARRAY1,JARRAY,FLGRAY,JRCD,JMAC,JMATYP,
 1 MATLAYO,LACCFLA)
  EPS11=ARRAY1(1)
  EPS22=ARRAY1(2)
  EPS33=ARRAY1(3)
  EPS12=ARRAY1(4)
  EPS13=ARRAY1(5)
  EPS23=ARRAY1(6)

  ! Obtain stress components
  CALL GETVRM('S',ARRAY2,JARRAY,FLGRAY,JRCD,JMAC,JMATYP,
 1 MATLAYO,LACCFLA)
  S11=ARRAY2(1)
  S22=ARRAY2(2)
  S33=ARRAY2(3)
  S12=ARRAY2(4)
  S13=ARRAY2(5)
  S23=ARRAY2(6)

  ! Load previous density (STATEV(1)) into Density
  Density = STATEV(1)

  ! Currently unused compensation for density dependent remodeling rate
  IF (Svflag.EQ.1) THEN
      S_v = -0.96285*Density**5+3.01439*Density**4-
 1            2.68758*Density**3-2.39079*Density**2+
 2            6.98199*Density-0.0195888
  ELSE
      S_v = 1.0
  ENDIF

! Calculating the strain energy density, using the stress and strain components
  Ua=S11*EPS11+S22*EPS22+S33*EPS33
  Ub=2.0*(S12*EPS12+S13*EPS13+S23*EPS23)
  U=0.5*(Ua+Ub)

  ! Calculating the local stimulus (SED/density)
  Stim = U/Density

  ! Storing the local stimulus of element NOEL
  Stimulus(NOEL) = Stim

  ! Obtaining the element numbers of nearby elements
  num_i = El_Num(NOEL,:)

  ! Obtaining the distance function values for the nearby elements
  f_i = El_Exp(NOEL,:)

 ! Obtaining the local stimulus function values for the nearby elements
  DO i=1,width
      S_i(i) = Stimulus(num_i(i))
  ENDDO

  ! Calculating the weighed stimulus for element NOEL
  sum_f_i = SUM(f_i)
```

```
      Stim_f_i = DOT_PRODUCT(f_i,S_i)
      PHI = Stim_f_i/sum_f_i

      ! Applying the lazy zone
      IF (PHI.LT.(1-lazy)*s) THEN
          DeltaDensity_i = B*(PHI-(1-lazy)*s)*DTIME
      ELSEIF (PHI.GT.(1+lazy)*s) THEN
          DeltaDensity_i = B*(PHI-(1+lazy)*s)*DTIME
      ELSE
          DeltaDensity_i = 0
      ENDIF

      ! Include effect of surface/area ratio on remodeling rate:
      !DeltaDensity_i = S_v*B*PHI*DTIME

      ! New density is equal to the old density plus the change in density
      NewDensity_i = STATEV(1)+DeltaDensity_i
      NewDensity = NewDensity_i

    ! If the density is either larger than rho_max or smaller than rho_min, it becomes equ
      IF (NewDensity_i.LE.0.01) THEN
          NewDensity = 0.01
      ELSEIF (NewDensity_i.GE.2.0) THEN
          NewDensity = 2.0
      ENDIF

    ! The state-dependent variable 1 value is equal to the new density (state-
dependent variable 1 is equal to the field variable)
      STATEV(1) = NewDensity
      FIELD(1)  = STATEV(1)

      ! This last section calculated the osteogenic index
      ! Obtain the principal stress components
      CALL GETVRM('SP',ARRAYSP,JARRAY,FLGRAY,JRCD,JMAC,JMATYP,
     1 MATLAYO,LACCFLA)
      SP1=ARRAYSP(1)
      SP2=ARRAYSP(2)
      SP3=ARRAYSP(3)

      ! Calculate the octahedral shear stress
      Ssi = SQRT((SP1-SP2)**2.0+(SP1-SP3)**2.0+(SP2-SP3)**2.0)/3.0
      ! Calculate the hydrostatic stress
      Shi = (SP1+SP2+SP3)/3.0

      ! Calculate the osteogenic index
      OI = a*Ssi+b*Shi

    ! Update the value of state-dependent variable 2 with the new osteogenic index
      STATEV(2) = OI

      RETURN
      END
```